

AD-A107 501

CAMBRIDGE UNIV (ENGLAND) DEPT OF METALLURGY AND MAT--ETC F/G 7/2
MICROHARDNESS, FRICTION AND WEAR OF SIC AND Si3N4 MATERIALS AS --ETC(U)
OCT 80 M G NAYLOR, T F PAGE

DA-ER0-78-6-010

UNCLASSIFIED

1 OF 1
AD A
1075 01

END
DATE
FILMED
12-81
DTIC

AD A107501

12.

LEVEL

IV

A091759

AD

MICROHARDNESS, FRICTION AND WEAR OF SiC AND
Si₃N₄ MATERIALS AS A FUNCTION OF LOAD,
TEMPERATURE AND ENVIRONMENT

SECOND ANNUAL TECHNICAL REPORT

By

M.G.S. Naylor and T.F. Page

October 1980

EUROPEAN RESEARCH OFFICE
United States Army,
London, NW1 5TH,
England.

DTIC
ELECTE
NOV 18 1981
B

GRANT NUMBER DA-ERO-78-G-010

University of Cambridge,
England.

Approved for Public Release; distribution unlimited

DTIC FILE COPY

81 11 16015

SECURITY CLASSIFICATION OF THIS PAGE (When Data Entered)

| REPORT DOCUMENTATION PAGE | | READ INSTRUCTIONS BEFORE COMPLETING FORM |
|---|--|--|
| 1. REPORT NUMBER | 2. GOVT ACCESSION NO. <i>AD-A107501</i> | 3. RECIPIENT'S CATALOG NUMBER |
| 4. TITLE (and Subtitle) MICROHARDNESS, FRICTION AND WEAR OF SiC AND Si ₃ N ₄ MATERIALS AS A FUNCTION OF LOAD, TEMPERATURE AND ENVIRONMENT. | | 5. TYPE OF REPORT & PERIOD COVERED Annual Technical Report, 1 October 79 - 30 Sep, 80 |
| 7. AUTHOR(s) M.G.S. Naylor and T.F. Page | | 6. PERFORMING ORG. REPORT NUMBER |
| 9. PERFORMING ORGANIZATION NAME AND ADDRESS Department of Metallurgy and Materials Science, University of Cambridge, Pembroke St., Cambridge. | | 8. CONTRACT OR GRANT NUMBER(s) DAERO-78-G-010 |
| 11. CONTROLLING OFFICE NAME AND ADDRESS | | 10. PROGRAM ELEMENT, PROJECT, TASK AREA & WORK UNIT NUMBERS |
| 14. MONITORING AGENCY NAME & ADDRESS (if different from Controlling Office) | | 12. REPORT DATE October 1980 |
| | | 13. NUMBER OF PAGES 63 |
| | | 15. SECURITY CLASS. (of this report) UNCLASSIFIED |
| 15a. DECLASSIFICATION/DOWNGRADING SCHEDULE | | |
| 16. DISTRIBUTION STATEMENT (of this Report) Approved for public release: distribution unlimited. | | |
| 17. DISTRIBUTION STATEMENT (of the abstract entered in Block 20, if different from Report) | | |
| 18. SUPPLEMENTARY NOTES | | |
| 19. KEY WORDS (Continue on reverse side if necessary and identify by block number) SiC, Si ₃ N ₄ , Si, single crystal SiC, hot-pressed SiC, sintered SiC, reaction-bonded SiC, pyrolytically-deposited Si ₃ N ₄ , hot-pressed Si ₃ N ₄ , reaction-bonded Si ₃ N ₄ , hardness, microhardness, temperature dependence of hardness, indentation plasticity, indentation fracture, fracture toughness, load sensitivity of hardness, impurity effects, surface finish effects. | | |
| 20. ABSTRACT (Continue on reverse side if necessary and identify by block number) see over | | |

UNCLASSIFIED

SECURITY CLASSIFICATION OF THIS PAGE(When Data Entered)

The microhardness and indentation fracture response of various microstructural forms of SiC, Si₃N₄ and also {111} single crystal Si have been studied using Vickers indentation techniques at temperatures ranging from 20-800°C and at applied loads of between 0.1 and 1 kgf, in vacuo. In all cases, examination of indented samples by optical and SEM methods has been used to establish the microstructural control of indentation fracture paths and surface deformation structures.

The Vickers hardness of SiC materials was found to decrease by ~60% between 0.1 and 0.35 T_m, whilst Si₃N₄ showed a decrease of ~30% over the range 0.15 - 0.5 T_m. Silicon carbide materials were generally harder than silicon nitrides at room temperature (only PDSN having comparable hardness), but the reverse was true at high temperatures (~600°C). {111} single crystal Si showed a 95% decrease in hardness between 0.2 and 0.6 T_m, a ductile-brittle transition occurring at ~600°C (0.5 T_m).

Microstructural influences on hardness were found in all materials, but were more pronounced in the nitrides examined than in the carbides. In general, single crystals or coarse-grained materials were harder than fine-grained materials over the whole temperature range. Porosity is thought to cause softening at low temperatures only. However, pores were also found to provide crack termination sites in some cases, and both grain boundaries and pores (often situated at the boundaries) formed preferred fracture paths, especially in fine-grained materials at high temperatures.

Cracking generally became more severe with increasing temperature, as reported previously (1), and this is explained in terms of recent theories of (radial) crack growth. The effect was most pronounced for {111} single crystal Si, followed by SiC materials, Si₃N₄ samples showing comparatively little change in crack extent with temperature. Crack nucleation became more difficult with increasing temperature.

Quantitative fracture parameters (K_{IC}, P*) have been calculated as a function of temperature and microstructure, and have been compared with bulk mechanical values and direct observations.

Effects of applied load, specimen impurity content and surface finish were also investigated.

| | |
|--------------------|-------------------------------------|
| Approved for | |
| By | <input checked="" type="checkbox"/> |
| Dist | <input type="checkbox"/> |
| Special | <input type="checkbox"/> |
| Availability Codes | |
| Dist | Special |
| A | |

UNCLASSIFIED

SECURITY CLASSIFICATION OF THIS PAGE(When Data Entered)

| <u>CONTENTS</u> | <u>PAGE</u> |
|--|-------------|
| Abstract | ii |
| Contents | iii |
| List of Figures | iv |
| List of Tables | v |
| 1. Introduction | 1 |
| 2. Plasticity in Ceramic Materials | 2 |
| 2.1. General | 2 |
| 2.2. Indentation plasticity | 4 |
| 2.3. Temperature effects | 6 |
| 3. Indentation fracture | 8 |
| 3.1. Crack Propagation | 8 |
| 3.2. Crack Initiation | 9 |
| 4. Experimental | 11 |
| 4.1. Materials | 11 |
| 4.2. Indentation Techniques | 12 |
| 5. Results | 13 |
| 5.1. Hot-Hardness | 13 |
| 5.2. Indentation fracture | 14 |
| 5.2.1. Crack propagation | 14 |
| 5.2.2. Crack initiation | 17 |
| 6. Discussion | 18 |
| 6.1. Hardness as a function of temperature | 18 |
| 6.2. Indentation fracture | 20 |
| 6.2.1. Crack propagation | 20 |
| 6.2.2. Crack initiation | 22 |
| 7. Conclusions | 23 |
| 8. Further work | 24 |

| <u>CONTENTS</u> (cont.) | <u>PAGE</u> |
|--|-------------|
| 9. Acknowledgements | 24 |
| 10. References | 25 |
| 11. Glossary | 32 |
| 12. Appendix 1. Hardness as a function of load | 33 |
| 13. Appendix 2. Hardness as a function of impurity content | 35 |
| 14. Appendix 3. Hardness as a function of surface finish | 37 |
| <u>FIGURES</u> | |
| Fig.1. The variation of Vickers hardness with temperature for SiC materials. | 49 |
| Fig.2. The variation of Vickers hardness with temperature for Si ₃ N ₄ materials. | 50 |
| Fig.3. The variation of Vickers hardness with temperature for n-type {111} single crystal silicon. | 51 |
| Fig.4. Fracture around Vickers indentations in Carborundum sintered SiC. | 52 |
| Fig.5. Fracture around Vickers indentations in 'Suzuki' sintered SiC. | 53 |
| Fig.6. Fracture around Vickers indentations in Ford '2.7' reaction-bonded Si ₃ N ₄ . | 54 |
| Fig.7. Indentation fracture in Norton NC132 hot-pressed Si ₃ N ₄ (MgO additive). | 55 |
| Fig.8. Indentation fracture in Norton NCX34 hot-pressed Si ₃ N ₄ (Y ₂ O ₃ additive). | 56 |
| Fig.9. Vickers indentations made at various temperatures on {111} single crystal Si (n-type) with one indenter axis parallel to <110>. | 57 |
| Fig.10. Radial crack radius as a function of temperature and load for SiC materials. | 59 |
| Fig.11. Radial crack radius as a function of temperature and load for Si ₃ N ₄ materials. | 60 |
| Fig.12. Radial and lateral crack radii as a function of temperature and load for n-type {111} single crystal Si. | 61 |
| Fig.13. The effect of including a plastic zone size term in the calculation of K_{IC} as a function of temperature in hot-pressed SiC. | 61 |
| Fig.14. The variation of 'index of brittleness' (H/K_{IC}) with temperature for SiC materials. | 62 |

| | | |
|---------|--|----|
| Fig.15. | The variation of 'index of brittleness' (H/K_{Ic}) with temperature for Si_3N_4 materials. | 62 |
| Fig.16. | The variation of 'index of brittleness' (H/K_{Ic}) with temperature for {111} single crystal Si. | 62 |
| Fig.17. | The temperature sensitivity of P^* , the critical load required for radial crack nucleation: SiC materials | 63 |
| Fig.18. | The temperature sensitivity of P^* : Si_3N_4 materials. | 63 |
| Fig.19. | The temperature sensitivity of P^* : {111} single crystal Si. | 63 |

TABLES

| | | |
|-------------|---|----|
| Table 1. | Properties of the materials investigated. | 39 |
| Table 2. | A summary of experimental work performed to date. | 41 |
| Table 3. | The ratio (b/a) of plastic zone radius to Vickers indentation radius at constant applied load (1 kgf) as a function of temperature for SiC and Si_3N_4 materials and {111} single crystal Si. | 42 |
| Table 4. | The ratio (c/a) of radial crack radius to Vickers indentation radius at constant applied load (1 kgf) as a function of temperature for SiC and Si_3N_4 materials and {111} single crystal Si. | 43 |
| Table 5. | The ratio (c/b) of radial crack radius to plastic zone radius at constant applied load (1 kgf) as a function of temperature for SiC and Si_3N_4 materials and {111} single crystal Si. | 44 |
| Table 6. | Indentation fracture toughness values for SiC and Si_3N_4 materials and {111} single crystal Si as a function of temperature. | 45 |
| Table A1. | Variation of Meyer index (n) with temperature for Vickers indentations in the load range 100 gf - 1 kgf. | 46 |
| Table A2.1. | The effect of dopant on the Vickers hardness of {111} single crystal Si as a function of temperature. | 47 |
| Table A2.2. | The effect of dopant on the room temperature Vickers hardness of α and β REFEL reaction-bonded silicon carbides. | 47 |
| Table A.3. | The effect of surface finish on the room temperature Vickers hardness of alpha REFEL silicon carbide. | 48 |

1.

1. INTRODUCTION

Engineering ceramics based on SiC and Si₃N₄ have been developed primarily for high-temperature applications such as gas turbine components (e.g. 2,3), but have also found increasing use as bearing and abrasion-resistant surfaces (2-5) due to their excellent (unlubricated) friction and wear characteristics in severe environments (6). It is this latter area of use which is of primary interest to the present program of research, though most of the results on microstructural characterization and control of deformation behaviour are of much wider significance to the general behaviour of SiC and Si₃N₄ ceramics.

Material loss in abrasive and erosive situations is controlled by some combination of fundamental deformation mechanisms, such as localized plasticity (e.g. 7) often coupled with various crack arrays in brittle solids (e.g. 8). These mechanisms are most conveniently investigated and quantified experimentally by means of indentation hardness tests, simple sliding stylus wear tests, etc., and previous research in Cambridge* (e.g. 9-11) has characterized the basic deformation behaviour and microstructural control of such properties at room temperature and under ambient conditions. Thus, the microstructures of several SiC and Si₃N₄ ceramics have been characterized (e.g. 12), hardness anisotropy and etching used to evaluate slip systems in SiC single crystal (e.g. 13,14), and the microstructural control of crack paths examined in a range of SiC and Si₃N₄ materials (9-11) - all at room temperature. Non-ERO-supported investigations in Cambridge have made parallel studies of the load dependence of hardness in ceramics (15,16) and the role of phase transformations in the microstructural development of SiC (17). The information which may be derived from indentation tests is reviewed in sections 2 (plasticity effects) and 3 (indentation fracture).

The aim of the current program is to determine the effects of important variables such as temperature and environment on indentation processes, and to characterize further the role of microstructure as a function of such variables. To this end, a variety of indentation techniques have been performed using a controlled-atmosphere, temperature-variable microhardness tester commissioned especially for this project (1,18,19). In parallel with these investigations, a wide range of optical, electron-optical and X-ray diffraction techniques are being utilized for the characterization of specimen microstructures and both surface and subsurface contact-induced deformation structures.

* Also supported by the European Research Office of the U.S. Army, 1973-76 (e.g. 20).

2. PLASTICITY IN CERAMICS

2.1. GENERAL

In this section, the term 'plasticity' is used loosely to refer to any irreversible deformation mechanism, excluding brittle fracture. A full review of plasticity in ceramics is not attempted here - the subject is immense and has been extensively reviewed elsewhere (e.g. 21-24). The purpose of this section is merely to provide a background to the more detailed discussions of indentation plasticity in SiC and Si₃N₄ materials presented later.

Plastic deformation may be divided into two broad categories, namely grain processes (including dislocation glide, climb, kinking and also twinning) and grain boundary processes (e.g. grain boundary sliding, diffusional and viscous creep). Grain processes will be considered first.

Dislocation activity is observed in all ceramics, albeit on limited slip systems (e.g. 25), for instance Si₃N₄ forms {10 $\bar{1}$ 0}[0001] dislocations (25, 26) which (if glissile) would produce 2 independent slip systems only. Secondary slip systems are as yet unknown. 6H* SiC shows prismatic slip ((10 $\bar{1}$ 0)<11 $\bar{2}$ 0>)(13,25) with basal ({0001}<11 $\bar{2}$ 0>)(13) secondary slip, which should produce a total of 4 independent shear strains if they act independently. Neither material satisfies the von Mises (29) criterion of 5 independent slip systems for a general small, homogeneous strain without change in volume. In principle, β -SiC*, in common with other sphalerite materials (e.g. diamond, Si, Ge), has twelve available {111}<1 $\bar{1}$ 0> slip systems, however the von Mises criterion is not satisfied until slip may occur homogeneously within each grain and the various slip systems may interpenetrate freely (30). All these materials are brittle at room temperature, the critical resolved shear stress (CRSS) for dislocation glide being large (e.g. 23).

High CRSS values in ceramics are a consequence of high Peierls stresses (37), dislocation pinning by, for example, vacancies or charged impurities (e.g. 31,32) and interactions with dislocations on parallel slip planes (e.g. 33). These factors arise from the nature of atomic bonding in ceramic materials, which gives rise to problems of charge neutrality in ionic solids and bond breaking and bending in covalent materials such as SiC and Si₃N₄. Dislocation structures in tetrahedrally co-ordinated cubic semiconductors (e.g. β -SiC) have recently been reviewed by Hirsch (34), who suggests that screw, edge and 60° dislocations are resolved into partials and that bond reconstruction may take place in the core structures of these partials, so that dangling bonds only occur at kinks, antiphase defects and possibly in the cores of 60° partials constituting edge dislocations.

Gilman (35, 36) has modelled low-temperature plastic flow in covalent solids as a process involving the formation and growth of kink pairs on dislocation lines by phonon-assisted tunnelling of bonding electrons into

*SiC displays a number of polytypic stacking sequences (27), one of which is cubic (β or 3C in Ramsdell notation), the rest being designated as α (hexagonal or rhombohedral) structures, the most common being 6H (28). Silicon nitride exists in two hexagonal crystalline polymorphs (α and β) (25).

the conduction band under the influence of the applied stress. Gilman's theory predicts both the flow stress (essentially the 'Peierls stress', although pinning by impurities may also be treated to give a 'friction stress') and the activation energy for glide ($\approx 2Eg$), both as a function of temperature up to some critical (stress-dependent) value at which conventional thermal activation begins. The Peierls mechanism in an ionic material (MgO) has been modelled by Woo and Puls (37) using atomistic calculations, again based on formation and motion of double kinks.

Work-hardening has been reported in ionic materials (e.g. 31, 32, 38, 39), mechanisms being either dislocation-dislocation dipole interactions (athermal) or dislocation-vacancy interactions (thermally activated), or both. High concentrations of both types of defect may be formed as 'dislocation debris' by cross glide of screw dislocations, which are much less mobile than edge dislocations at low temperatures (31, 32). Temperature effects are more fully discussed in section 2.3.

Finally, on the subject of dislocation glide, it is worth emphasizing that limited slip may actually nucleate cracks (40), for instance at the intersection of slip bands with grain boundaries (41-43) or by slip band interaction (44, 45). The potential role of plasticity in crack propagation has been recently reviewed (46), with the conclusion that cracks formed at room temperature in SiC, Si, Ge and Al_2O_3 are atomically sharp, and propagate by sequential bond rupture rather than by microplasticity. At 500°C, on the other hand, Si showed substantial crack tip plasticity. Koss and Chan (47) have studied fracture along planar slip bands in Ni-, Al- and Ti- base alloys, and have shown that this may hinder the activation of non-coplanar secondary slip and provide relatively easy crack paths. This observation may have wider significance for ceramic materials, where slip planes are often cleavage planes also.

Twinning - another potentially important grain deformation process - is observed in some materials, e.g. Al_2O_3 (48) and Si (beneath Vickers indentations made between 350 and 650°C (49)). Twinning may or may not produce strain, and may cause premature fracture due to stress concentration if not accommodated by other mechanisms (24).

Whilst grain processes have received most attention in previous fundamental studies of deformation in ceramics, grain boundary processes are relatively not well understood. This is unfortunate, since such processes dominate under many conditions of applied stress/strain rate/temperature. Studies of grain boundary processes are hampered by the relative lack of information on boundary structure, which has only been characterized for certain ceramics (e.g. 26, 50-60), especially hot-pressed materials where thin (10-20Å) glassy films have been observed (e.g. 52-57) along boundaries and especially at triple grain junctions.

Grain boundaries are known to play a particularly significant role in high temperature processes such as creep: Coble creep involves mass transport along boundaries from compressive to tensile regions, and has been postulated in SiC above 1900°C (62). Nabarro-Herring creep involves mass transport through grains with the boundaries acting as vacancy sources/sinks.

Creep by high temperature grain boundary sliding accompanied by viscous and/or diffusive growth of grain boundary cavities has been modelled by Evans and Rana (61) for materials with or without amorphous boundary phases. This leads to the concept of grain boundary 'engineering' in order to reduce creep rates, either by making boundary phases more refractory (e.g. in Y_2O_3 hot-pressed Si_3N_4 (63)) or by eliminating them altogether (e.g. by prolonged heat treatment to desegregate boundaries in SIALON materials (58)). In the absence of boundary phases, creep occurs by a non-cavitating diffusional (Coble) mechanism (58).

High temperature subcritical crack growth often involves viscous cavity nucleation (and growth) by grain boundary sliding ahead of the primary crack tip (64). (In the absence of boundary glass phases, slow crack growth perhaps involves thermally-activated intergranular bond rupture at the crack tip, or diffusion-controlled cavity growth from triple junctions (58)). Although boundary sliding is necessary for cavity nucleation, it is not necessarily the rate-limiting step (65). In some temperature régimes boundary sliding may cause crack blunting to occur, decreasing the rate of slow crack growth (64).

Whether grain boundary sliding, in its own right, may be considered a deformation mechanism contributing plastic strain is reviewed by Dokko and Pask (24), the conditions for such a contribution being unclear. Grain boundary sliding in MgO above $1700^\circ C$ has been described in detail by Day and Stokes (66). Porosity was found to promote sliding by (a) providing the source, (b) decreasing the interfacial contact area and (c) preventing grain boundary migration, which produces corrugations in the interface which interfere with sliding. Boundary migration may, in other systems, act to relieve stress concentrations caused by sliding, and may also facilitate slip transfer across boundaries (24). The effect of sliding and migration on grain boundary structure is unclear.

An interesting observation is that grain boundaries in MgO may initiate dislocations at a stress independent of grain size and below the microyield stress (67). It is uncertain whether this effect occurs generally.

To summarize, plastic deformation may take place by grain or grain boundary processes, which may act independently, co-operatively or even competitively. There is a great need for further investigations of both the processes themselves and their interactions with each other, as a function of both material and environmental parameters (e.g. microstructure, impurity content, environmental chemistry) and external variables (e.g. applied stress, strain rate, temperature).

2.2. INDENTATION PLASTICITY

The subject of indentation plasticity has been extensively reviewed by various workers (e.g. 13, 15) and by the present authors (1), and so will not be discussed at great length here.

The deformation mechanisms which operate in response to indentation must be related to the materials parameters and external variables previously mentioned. In particular, the applied stresses in indentation tests are generally far larger than in other mechanical tests, and are both highly localized and also highly complex.

Solutions exist for elastic stress fields beneath blunt (Hertzian) and sharp (Boussinesq) indenters (e.g. 68), but elastic/plastic indentation stress fields have not yet been completely characterized. The most widely-adopted model for plastic zone effects is the spherical cavity model due to Hill (69), which has been coupled with the elastic solution by Evans (70), with a view to describing indentation fracture behaviour. However, the effects (which must be considerable) of fracture on the sub-indentation stress field have not, to the authors' knowledge, been considered at all. To generalize, the stress field contains large, localized shear components (giving rise to slip), together with local hydrostatic compression (inhibiting massive cracking) and tensile stresses (maximum at the elastic/plastic zone boundary on the load axis (70), which may propagate a number of crack geometries (see section 3).

It has been established by a wide variety of techniques (e.g. TEM (7, 9, 46, 71-77), etch-pitting (14, 77-80), cathodoluminescence (15, 77), SEM (1, 81) and selected area electron channelling (82)) that even the most brittle materials exhibit some form of slip response, however localized, to surface contact situations involving sharp indenters. Some observations suggest that indentation hardness is highly dependent on slip processes - for instance, single crystal hardness anisotropy is clearly related to active slip systems (e.g. 13, 83), and work-hardening of MgO by repeated sliding of softer styli across the surface results in higher hardness values (79, 80). In other cases, slip does not provide a complete explanation of observations - for example, hardness is independent of pre-existing dislocation density in mixed KCl-KBr crystals (84) and in sapphire (85), which has, if anything, a relatively high hardness at very low dislocation density. Dislocation mobilities are also thought to be too low to account for deformation of silicon at low temperatures (75). In summary, the precise role of slip has yet to be established, although it has been conjectured (13, 15) that in highly brittle solids, slip may accommodate material displaced by other deformation mechanisms (discussed below).

Twinning has been observed to occur beneath Vickers indentations in Si in the temperature range 350-650°C (49), and may well occur in SiC materials, in which stacking fault energies are very small indeed (17).

Grain boundary sliding has recently been identified as the major deformation mechanism beneath indentations in ZnS (81), with deformation (slip or twinning) also occurring within the grains. Voids were formed due to both gross boundary sliding and either interaction between, or continued slip along, shear flow lines observed within the highly deformed regions beneath indentations.

It has been suggested (e.g. 13, 75) that shear stresses beneath an indenter may in some cases exceed the theoretical shear strength for the test material, giving rise to block shear, especially near the tip of the indenter at the beginning of indentation (13).

Finally, a pressure-sensitive densification mechanism has been proposed for sphalerite (zinc-blende structure) crystals such as diamond, Si, Ge, InSb (86). At temperatures below $\sim 0.3 - 0.4 T_m$, where hardness is only weakly temperature dependent (see section 2.3), the hardness is thought to be of the order of the transition pressure required for localized formation (due to the high hydrostatic pressure) of a dense metallic phase beneath the indenter. Trefilov et al. (87)

have tentatively suggested that SiC may exhibit similar behaviour, whilst Velednitskaya et al. (77) have postulated a similar mechanism in materials with the NaCl structure. This aspect is more fully discussed by Sawyer, Sargent and Page (13) in the context of the hardness anisotropy of SiC.

2.3. TEMPERATURE EFFECTS

Most brittle solids show two régimes of hardness behaviour: at low temperatures (below $\sim 0.2 - 0.5 T_m$, depending on the material) hardness is only a weak function of temperature (e.g. 88, 89) and dislocations, although produced, do not extend far from the indentation (e.g. 7, 9, 46, 49, 71-77). At higher temperatures, hardness decreases strongly with increasing temperature and dislocations may move over considerable distances (e.g. 49).

The form of the hardness/temperature curve is often similar in form to those of f.c.c. metals (reviewed in references 88, 90, 91), which generally have two régimes: below $0.5 T_m$, the hardness falls relatively slowly with increasing temperature, whereas above $0.5 T_m$ the decrease is more rapid. In the low-temperature region, hardness depends on glide processes and, since dislocation mobilities are high, the flow rate is limited by strain-hardening effects (92). Dislocation-dislocation interactions are elastic and long-range in f.c.c. metals, and are therefore only weakly dependent on temperature (92). Above $0.5 T_m$, the deformation is diffusion-controlled (93, 94), involving, for example, dislocation climb and grain boundary sliding: below $\sim 0.75 T_m$, dislocation pipe-diffusion is thought to be dominant, whilst at very high homologous temperatures, lattice diffusion dominates (91).

The form of the hardness/temperature relationship is the same, for different reasons, in covalent semiconductors such as Si, Ge, InSb (49, 86, 95), the low-temperature region being totally athermal. Whilst the high-temperature régime is thought to be controlled by dislocation processes (49, 86), the low-temperature region is clearly not (by comparison with the form of the temperature-dependence of the CRSS for dislocation glide). The CRSS is generally highly temperature and strain-rate sensitive at low temperatures, dislocations being trapped by obstacles in the glide-plane having short-range stress fields (e.g. solute atoms or the Peierls barrier) (31-33). At intermediate temperatures, the CRSS is athermal (long-range interactions) and at high temperatures it is diffusion controlled, hence thermally activated (33). Therefore, if the high-temperature régime in the hardness-temperature relation is controlled by slip, it is in the diffusion-controlled region. In this temperature domain, creep effects must be taken into account - the subject of indentation creep has been reviewed extensively elsewhere (e.g. 89, 96) and will not be further discussed here, since all experiments described in this report were at short indenter dwell-times, at temperature where creep effects are known to be minimal.

For Si, etc., the low-temperature hardness régime has been explained in terms of a pressure-induced phase transition mechanism (mentioned in section 2.2) by Gridneva et al. (86). Gilman (35, 36) has postulated an entirely different mechanism, involving escape of dislocations from bound states by electron tunnelling, to account for low-temperature, non-thermally-activated flow (hence hardness, since

H α flow stress) of covalent solids (see section 2.1). The model fits the observed form of the hardness/temperature curve for Si nicely (36), but takes no account of the physical movement of atoms, and is difficult to use since the nature of the potential energy barrier, through which tunnelling takes place, is not known in detail (75). Hill and Rowcliffe (75) have further suggested that block shear may be the dominant deformation mechanism in the athermal region of the hardness/temperature curve for Si.

Not all materials exhibit the form of temperature response described earlier: notable exceptions are the transition metal carbides, which generally show a steep decrease in hardness with increasing temperature up to $\sim 0.2 T_m$, where the decrease becomes even steeper (88-90, 97, 98). Single crystal hardness anisotropy experiments (using the theory of Brookes et al. (83)) have established that a change in slip system (from $\{110\}\langle 1\bar{1}0\rangle$ to $\{111\}\langle 1\bar{1}0\rangle$) occurs at this point (89, 99-102), corresponding to a change in atomic cohesion from covalent at low temperature to metallic at high temperature (103, 104).

The hardness/temperature behaviour of silicon carbide has been reported to show a low-temperature athermal region which only extends up to 400°C ($\sim 0.2 T_m$) (Berkovich indenter (87)) or 200°C ($\sim 0.15 T_m$) (Knoop indenter (1)). Vickers hardness data show no such region above room temperature ($\sim 0.1 T_m$) (1, 105, 106). Above these temperatures, all investigations revealed a marked decrease in hardness with increasing temperature, with gross plasticity (in the form of surface slip steps around indentations) not occurring below 800°C (1, 105), and with apparently no change in slip system taking place (at least, below 1500°C) (105). Although Trefilov et al. (87) have suggested that this behaviour may be similar to that of Si, clearly some explanation is required for the athermal region ending at such a low homologous temperature.

Silicon nitride, on the other hand, has been reported to have only a comparatively weak temperature-dependence of hardness up to very high temperatures, single crystals of $\alpha\text{-Si}_3\text{N}_4$ showing no sign of a knee in the curve below 1500°C ($0.8 T_m$) (107), although some hot-pressed materials show a rapid decrease in dynamic hardness above 1300°C ($0.7 T_m$) (108).

The data of Huseby and Petzow (108) are interesting, as they show clear differences in the hot-hardness behaviour of various hot-pressed silicon nitrides as a function of pressing additive (hence grain boundary phase). Similar results were obtained by Loladze et al. (106) for Al_2O_3 materials with various additives. These differences may be significant in the light of recent observations (81) that grain boundary sliding may make a major contribution to indentation plasticity, even at low temperatures.

Porosity effects have been discussed by various authors (e.g. 1, 88, 89, 97, 109, 113) and are thought to give rise to softening at low homologous temperatures but, at higher temperatures, the hardness is found to be independent of porosity.

The effects of adsorbed species, especially water, on hardness (and other) properties of ceramic materials is well-established (e.g. 110-112): both softening and anomalous room temperature creep of surface layers is observed. For materials prone to such chemomechanical effects, thermal desorption of adsorbed species will result in changes in hardness behaviour in addition to the variations discussed above. All experiments here were performed in liquid nitrogen-trapped high vacuum ($<10^{-6}\text{ mmHg}$) in order to eliminate these effects as far as possible.

3. INDENTATION FRACTURE

3.1. CRACK PROPAGATION

Indentation fracture geometries have been characterized and modelled principally by Lawn, Evans and co-workers (e.g. 68, 114-116): in the case of sharp surface contact, cracks perpendicular to the specimen surface (median cracks) are created during loading, cracks approximately parallel to the test surface (lateral cracks) being created during unloading. More complex geometries (such as radial cracks, which may form an unloading or loading or both) have also been observed (116-119). It has been established that the incidence of lateral fracture in particular (116), combined with other crack types, plays a dominant role in abrasive and erosive wear of brittle materials, and that with increasing load, a transition from plasticity control to fracture control of abrasive wear is observed (74, 120).

The precise sequence of microfracture events depends on the material, its surface preparation and the applied load (35), and it would appear that radial cracks are generally the first to form around Vickers indentations in SiC (82). The microstructural dependence of indentation fracture, in terms of preferred fracture paths, may easily be investigated by direct examination of indentations in a range of materials, enabling conclusions to be drawn as to materials response to abrasive environments, and this has been one of the principal interests of the authors and co-workers (1, 9-11).

A quantitative fracture mechanics model for the dependence of radial/median crack extent on contact load has been developed (121-123) by considering the interaction of the tensile component of the sub-indentation stress field with pre-existing flaws within the test material. For median crack propagation, the following relationship was obtained:

$$a) \quad K_{Ic} = \frac{Pc_m^{-3/2}}{\beta_o} \quad (\text{for explanation of terms, see glossary})$$

where $\beta_o \sim 7$

The effects of the plastic zone in modifying stress fields, and hence fracture behaviour, have been discussed by Evans (70). From this, a more reasonable model for the propagation of median and radial cracks under the appropriate loading and unloading stress fields has recently been developed (124). The complex elastic/plastic stress field beneath the indenter is resolved into elastic and residual components (125) - the elastic reversible component is responsible for downward median crack extension during loading whilst the residual stress, arising out of the mismatch between the plastic zone and the surrounding elastic matrix, provides the driving force for radial crack extension during unloading. Thus, the final measured radial crack length (c_r) at complete unloading is governed by the crack-opening force provided by the residual stress component, and the relationship between c_r and applied load P is modified:

$$b) \quad K_{Ic} = \chi_r P c_r^{-3/2}$$

$$c) \quad \chi_r = \xi_r(\phi) (E/H)^{1/2} (\cot \psi)^{2/3}$$

where $\xi_r(\phi)$ is a dimensionless term independent of the indenter/specimen system, found by experiment (124) to be $0.032 (\pm 0.002)$.

ψ = indenter half-angle (74° for a Vickers indenter)

Hence, for Vickers indentations:

$$d) \quad K_{Ic} = \frac{0.0139 (E/H)^{1/2} P}{(\pm 0.0009) c_r}^{-3/2}$$

In this treatment, $(E/H)^{1/2}$ is a measure of the ratio (b/a) of plastic zone radius to indentation radius, derived from the expanding cavity model due to Hill (69). Thus it is apparent that as the temperature is raised, the ratio (b/a) must increase, causing a larger crack-opening residual stress and therefore an increase in radial crack extent, as has been observed (1, 87). An interesting observation here is that as the ratio (H/E) diminishes by, for example, considering a range of materials (116) or one material at various temperatures (126), the surface radial component progressively dominates the subsurface median cracks in the earlier stages of loading, although the same near-semicircular profile is almost invariably attained on removal of the load (124).

It must be emphasised that the theory of Lawn et al. is strictly valid only for conditions in which $c_r > b$, i.e. that the radial cracks are driven into the elastic hinterland by the residual stress. This may not be the case for low applied loads and relatively soft materials, for which the model due to Perrott (119) may be more applicable. This model predicts that the first cracks to form, under conditions of sufficient plasticity, are surface radial cracks, for which the Palmqvist relationship Pac_r often holds, as has been observed in various WC/Co materials (127). Whilst Lankford and Davidson (82) have suggested that this behaviour occurs in SiC (4H single crystal), their numerical results are entirely consistent with the Lawn et al. model discussed above. $c_r P^{0.67}$ may be verified from their figure 4 (predicting $K_{Ic} = 1.8 \text{ MPa m}^{1/2}$, assuming $E = 450 \text{ GPa}$ (table 1)), as opposed to the $c = c^* + \text{constant} \cdot (b - b^*)$ relationship they propose (where c^* and b^* are threshold values of c and b respectively). The data of Lankford and Davidson confirm the Hill (69) relationships $a \propto b$ and Pab^2 , but the value of $(b/a) = 2.9$ which may be calculated from their results (again, assuming $E = 450 \text{ GPa}$) is lower than their observed value (using selected area electron channelling) of ~ 5.5 .

In summary, indentation techniques provide a useful (if theoretically complex), non-destructive experimental means of studying fracture in brittle materials or, for example, explaining strength-degradation after surface contacts (125). Quantitative results for crack propagation and initiation may easily be obtained as a function of specimen microstructure, temperature, environment, etc. In addition, such experiments are invaluable in allowing preferred fracture paths through specimen microstructures to be examined.

3.2. CRACK INITIATION

Crack initiation in elastic/plastic indentation fields was first considered by Lawn and Evans (122), using a simple approximation for the tensile stress distribution beneath an indenter (again, based on Hill's solution (69)) and the interaction of this stress (which scales with hardness and is a maximum in the vicinity of the elastic-plastic boundary (70)) with pre-existing flaws in the test material. Threshold conditions of applied load (P^*) and critical pre-existing flaw size (c^*) were derived, below which

no median cracks could form:

$$e) \quad P^* = \lambda_0 (K_{IC}/H)^3 K_{IC} \quad \text{where } \lambda_0 \text{ was estimated to be } \sim 2.2 \times 10^4$$

$$f) \quad c^* = \mu_0 (K_{IC}/H)^2 \quad \text{where } \mu_0 \text{ was estimated to be } \sim 442$$

In this model, if no large ($c > c^*$) flaws are present in the vicinity of the plastic zone boundary, the applied load has to be increased so that the expanding tensile front may sample deeper-lying flaws, in order to form a median crack. The coefficients λ_0 and μ_0 were later modified (123) to fit a wide range of experimental data giving $\lambda_0 \sim 1.6 \times 10^4$, $\mu_0 \sim 120$, however the theory was considered too inexact to enable absolute results to be derived to within an order of magnitude.

More recently, Hagan (45) has shown that pre-existing flaws are not necessary for crack formation, rather the flaws may be nucleated by the deformation processes occurring during indentation (thus removing the c^* criterion for nucleation). Hagan's analysis, based on crack nucleation by intersection of dislocations on two intersecting slip planes, or by one slip plane blocking another, enabled a critical load for nucleation to be derived, which followed the form of the earlier result, with only a difference in the coefficient λ_0 (~ 885 in this case). Nucleation was thus considered to be governed by shear deformation rather than tensile stresses as described above. Such dislocation-induced fracture has been specifically observed in nucleation of $\{112\}$ cracks on near $\{111\}$ Si (128), and has been considered in general terms by Davidge and Evans (40).

A similar mechanism was also postulated for soda-lime glass (44, 45), in which cracks are observed to nucleate at the intersections of inhomogeneous shear bands formed in the deformed regions beneath Vickers indentations (123). Such flow lines have also been observed in ZnS, where cavities produced as a result of grain boundary sliding may also act as crack nuclei (81).

In polycrystalline materials, fracture may also be initiated by dislocation pile-up at grain boundaries, as has been demonstrated for MgO bicrystals (41-43). In such cases, the relationship

$$g) \quad \sigma_F = \sigma_0 + KD^{-1/2}$$

is obtained, where σ_F = stress to form a crack, σ_0 = stress required for dislocation multiplication (rather than the friction stress), K = a qualitative measure of the effective cohesive strength at the glide band tip (boundary cohesion) and D = glide band length. Both σ_0 and K decrease with increasing temperature, but the stress concentration at the boundary decreases due to increasing glide band width and lower dislocation density (42). Hence the temperature-dependence of σ_F (hence P^*) is unpredictable.

11.

4. EXPERIMENTAL

4.1. MATERIALS

The materials used in this investigation were commercially available forms of polycrystalline silicon carbide and silicon nitride, plus a large (0001) single crystal SiC, and these are listed in table 1, together with some room temperature properties obtained from the literature.

Sections of each of the polycrystalline samples were cut using a high-speed diamond saw (12) and these, together with a selected as-grown basal habit single crystal SiC, were mounted in electrically-conducting resin and diamond lapped and polished to 0.25 μ m finish (see Appendix 3). Specimens were examined optically and by SEM, for which the nitrides were lightly gold-coated and viewed at normal incidence, so as to image the material through the coating. Porosity and residual Si content (in REFEL) were measured directly from optical images by a Quantimet 720B image analyzer and grain sizes were estimated from SEM images. Notable microstructural features are discussed below and in the previous report (1).

One form of 'Suzuki' sintered SiC was observed to consist of needle or plate-like grains of approximate length 20 μ m and width 2 μ m, with substantial (9 vol.%) porosity (fig. 5). The material was sintered with additions of B and C, and reportedly contains no grain boundary phases (130).

Ford '2.7' RBSN contained many pores, varying in size, and distributed inhomogeneously through the microstructure, with some regions relatively pore-free and other regions containing large pores (fig. 6 and (132)).

Norton NC132 hot-pressed Si₃N₄ contains ~5%MgO (pressing additive) (132) and is almost pore-free (fig. 7). Secondary and backscattered SEM images reveal specular white particles, apparently distributed around ~5 μ m sized grains. Energy dispersive X-ray analysis (Link 860) of these particles shows them to be rich in W, Si and often Fe and/or Ni. The presence of such particles has been reported previously (e.g. 65), and they are presumed to originate from the ball-milling stage in the fabrication procedure.

Norton NCX 34, containing 8% Y₂O₃ (132), was found to contain W-rich particles similar to those in NC132, but secondary electron images (fig.8) also revealed diffuse light patches around each grain, thus delineating the grain structure much more clearly, revealing occasional large (~20 μ m) grains. The light regions were found by EDX analysis to be rich in Yttrium, presumably as Y₂O₃, and high magnification images (e.g. fig. 8f) revealed what appeared to be networks of this phase running through the microstructure.

The Si single crystals were in the form of standard transistor-grade {111} wafers, polished on one side, and were indented in the as-received condition. Regrettably, no information was provided as to the nature and concentration of the dopants used, save that the resistivity of the p-type wafer was 7.05 Ω cm and that of the n-type material was 9.15 Ω cm

4.2. INDENTATION TECHNIQUES

Hot-hardness experiments were carried out in a Wilberforce Scientific Developments high-temperature microhardness tester as described in detail in the previous report (1). All experiments were carried out 'in vacuo' to prevent furnace oxidation and indenter graphitization and to exclude, as far as possible, any environmental or 'Rebinder' effects which are important in some ceramic materials (e.g. 110-112).

The experiments performed are summarized in table 2 - in all cases the loads used were 100, 200, 500 and 1000gf, with a constant indenter dwell time of 15s. Generally, 5 indentations were made at each of the lower loads, 10 at 1000gf. Measurements were made over the temperature ranges indicated at 100°C and 200°C intervals (as considered appropriate), with at least half an hour being allowed for stabilization of indenter and specimen temperatures prior to indentation.

As previously described (1) the (0001) single crystal SiC was indented with one Vickers indentation diagonal approximately parallel to a $\langle 11\bar{2}0 \rangle$ direction (Knoop experiments will not be described here). Similarly the {111} single crystals of Si were aligned such that one indentation diagonal was approximately parallel to a {110} direction. In all cases, indentations were observed at temperature and subsequently examined both optically (Zeiss Universal) and by scanning electron microscopy (ISI 100A) as in section 4.1.

The variations of radial crack extent with applied load and temperature were analyzed in accordance with the theories described in section 3. Firstly, the slope (m) of the $\log c$ versus $\log P$ plot was determined in each case: a value of $m = 2/3$ indicating $P \propto c^{3/2}$ (the Lawn et al. case (124)), a value of $m = 1$ indicating $P \propto c$ (the Palmqvist case (127)). With one exception (NCX 34 hot-pressed Si_3N_4), m was found to lie between 0.6 and 0.75 (± 0.03) and so the analysis due to Lawn, Evans and Marshall (124) was used-equation d (section 3.1). For this, the slope of the $c^{3/2}$ versus P plot was determined using the method of least squares, minimizing the variances in the experimental observation $c^{3/2}$, not those in the load P . Hardness values used in equation d were averaged over the load range over which cracks could be measured (H was often found to be slightly load dependent in this range). Room temperature values of Young's modulus are summarized in table 1 - in the case of 'Suzuki' sintered SiC, E had to be estimated according to the known variation of elastic modulus with porosity for SiC materials (25). In many cases, the temperature-variation of E has been measured (e.g. 25), but where such data were unavailable, a decrease of 1% per 100K temperature rise was assumed (e.g. 109).

Finally, values of P^* were calculated according to equation e (section 3.2), using a value of the constant λ_0 which best fitted the observed data (see section 5.2.2).

5. RESULTS

NB In this section, results are presented for all the materials investigated to date, including some which have appeared in the previous annual technical report (1). The variation of hardness with applied load (as a function of temperature) is described in Appendix 1, whilst dopant effects are discussed in Appendix 2 and surface finish effects in Appendix 3.

5.1. HOT HARDNESS

Figure 1a shows the Vickers hardness of SiC materials at 1 kgf applied load as a function of temperature in the range 20-800°C ($(T/T_m) \sim 0.1-0.35$). Broadly, the hardness/temperature curves are similar for all materials, the differences in microstructure merely transposing the curves up or down the hardness axis. The hardness of SiC materials thus falls from $\sim 2400-3200 \text{ kgfmm}^{-2}$ at room temperature to $\sim 800-1400 \text{ kgfmm}^{-2}$ at 800°C: a significant decrease. (0001) single crystal SiC was the hardest material over this temperature range, followed by NC203 hot-pressed and Carborundum sintered materials (curves almost indistinguishable), followed by the 'Suzuki' sintered SiC and finally REFEL reaction-bonded SiC.

Plotting these data on a logarithmic scale (figure 1b) reveals the decrease in hardness to be exponential, with constant activation energy over this temperature range, the exception being the reaction-bonded material, which contains unreacted silicon (see below and section 6.1). Otherwise, microstructural differences appear to have very little effect on the activation energy, the curves being transposed vertically from each other but not differing in slope.

Similar plots for silicon nitride materials are given in figure 2 on identical scales to those of figure 1. By comparison, Si_3N_4 materials show relatively little change in Vickers hardness with increasing temperature over this temperature range ($(T/T_m) \sim 0.15-0.5$); in addition, the effect of microstructural variation was much more pronounced for the nitrides.

PDSN was the hardest form of nitride investigated: its room temperature hardness ($\sim 3100 \text{ kgfmm}^{-2}$) being comparable to that of SiC materials. Although the temperature sensitivity of hardness was more marked for PDSN than for the other forms of Si_3N_4 , it was small compared to that of the carbides: at 800°C, the hardness of PDSN was $\sim 2100 \text{ kgfmm}^{-2}$. Much softer than PDSN were the two hot-pressed nitrides: NC132 (with MgO) and NCX34 (with Y_2O_3) - room temperature hardness values 2000 and 1700 kgfmm^{-2} respectively. This difference ($\sim 300 \text{ kgfmm}^{-2}$) was maintained over the whole temperature range, the forms of the two curves being very similar. Although the reaction-bonded material was the softest form of silicon nitride at room temperature, the material displayed a remarkable insensitivity of hardness to temperature, such that at 800°C its hardness value of 1300 kgfmm^{-2} was similar to that of the harder form of hot-pressed silicon nitride (NC132).

The logarithmic plot (figure 2b) suggests that the curves in figure 2a are exponential, each material maintaining a constant activation energy over the temperature range. In contrast to the carbides, different microstructural forms of silicon nitride show different slopes, RBSN having

the least and the two hot-pressed materials the greatest.

Figure 3a shows the variation of Vickers hardness (at 100gf applied load) with temperature for {111} single crystal silicon (n-type) over the range 20-800°C ($T/T_m \sim 0.15-0.65$). The decrease in hardness is both steep and approximately linear up to 500°C, where the decrease starts to tail off. Plotting the results on a logarithmic scale (figure 3b) produces a curve of gradually increasing slope, similar in shape to those obtained by other workers (e.g. 95), although transposed to higher hardness values. Slip steps along $\langle 110 \rangle$ directions were observed to form spontaneously around indentations made at and above 600°C (figs. 9 i-k) and indentations made at lower temperatures were observed to form slip steps on heating to this temperature. Slip steps were also formed at 500°C, but over a time scale of a few minutes (forming more readily around high-load indentations) (figs. 9 g, h).

The ratio (b/a) of plastic zone radius to indentation radius (for 1kg indentations) has been calculated (section 3.1) as a function of temperature for each of the materials investigated (table 3). At room temperature the plastic zone radius is calculated to be in the range 2.3a-2.7a for both SiC and Si₃N₄ materials (except PDSN: (b/a) ~ 1.9). The ratio increases (linearly in most cases) as the temperature is increased, the SiC materials showing the most pronounced change such that, at 800°C, (b/a) lies between approximately 3.5 and 4 for the carbides and between approximately 2.5 and 3.5 for the nitrides. Reaction-bonded SiC shows a comparatively rapid increase in plastic zone size ((b/a) ~ 4.7 at 800°C). {111} single crystal Si shows an increasingly rapid rise in (b/a) with increasing temperature, the theory predicting (b/a) ~ 8.4 at 800°C. It was found impossible to measure 1 kgf indentation sizes in silicon below 300°C, due to excessive fracture around the indentation profile (figs. 9a-d).

5.2. INDENTATION FRACTURE

5.2.1. CRACK PROPAGATION

In this section are presented, firstly, descriptions of the crack patterns (figs. 4-9) observed in the materials investigated since the first annual technical report (1) and, secondly, crack measurements (figs. 10-12) and derived values (figs. 13-16 and tables 4-6) for all the materials studied to date, as a function of temperature. Previously (1), Carborundum sintered SiC was shown to produce relatively little fracture (mostly lateral) around Knoop indentations over the whole temperature range. Around Vickers indentations, this material formed extensive radial cracks (fig. 4a) with only occasional lateral chips, radial fracture becoming more severe at high temperatures (fig. 4c). Cracks paths were sometimes branched, in many cases appearing to pass preferentially along grain boundaries for parts of their lengths. Often, cracks appear to have changed direction in order to pass through pores, which sometimes (by no means always) acted as termination sites (fig. 4c). Slip steps were observed to form in grains immediately adjacent to indentations made at 800°C (fig. 4d). By comparison the sintered SiC obtained from Prof. Suzuki formed shorter radial cracks, which were generally straight, passing non-preferentially through several pores over their lengths (figs. 5a, b). Sometimes, where the needle-like grains were suitable oriented, cracks propagated along grain boundaries (figs. 5c, d).

The RBSN specimen formed radial cracks at loads of 500 gf and above (figs. 6 a, c), no lateral fracture being observed. Crack paths were generally free from branches or major deflections, but appeared a little 'meandering', probably around the $\sim 1\mu\text{m}$ sized grains. The cracks were often associated with the substantial (intergranular) porosity in the material (figs. 6 b, d), and were sometimes terminated by pores.

The fully-dense NC132 hot-pressed silicon nitride (with MgO pressing additive) produced comparatively short radial cracks (figs. 7 a,c) at and above 500 gf load, the cracks being macroscopically straight but 'meandering' on a submicron scale (fig. 7b). The grain boundary WC/WSi particles were often seen to deflect cracks, and to provide both preferred fracture paths and occasionally, termination sites. These observations suggest that the crack paths were largely intergranular. At high temperatures, small intergranular lateral crack networks (similar to those observed in NC203 hot-pressed silicon carbide (1)) were observed (fig. 7d) together with short radial cracks at 1 kgf applied load. Below this load, the radial cracks were either absent or too small to be distinguishable.

The fracture behaviour of NCX 34 hot-pressed silicon nitride (with Y_2O_3 pressing additive) was similar to that of NC132 but more pronounced, radial cracks being measurable over the whole load range at all temperatures. Again, cracks were meandering (figs. 8a, c) and in this case clearly intergranular (figs. 8 b,d,e, f). At 800°C , networks of grain boundary cracks were formed (figs. 8d, e), more extensively than in NC132, but not as pronounced as in NC203 hot-pressed SiC (1).

Indentation fracture in {111} single crystal Si was generally spectacular at low temperatures (figs. 9 a-j), with extensive radial cracking occurring up to 700°C and severe lateral cracking up to 400°C . Lateral fracture was found to be favoured at low temperatures, being most severe at $\sim 200^\circ\text{C}$ (fig. 9d) and at high applied loads (figs. 9b, c), also at very high temperatures (e.g. 800°C) - where no radial fracture was present - in the form of small cracks and chips around/inside the indentation profile (figs. 9k, l). Radial cracks around high temperature ($500\text{--}700^\circ\text{C}$) indentations generally extended slightly beyond the slip steps which formed along $\langle 1\bar{1}0 \rangle$ directions at temperatures of 500°C and above, as described in the previous section. The radial cracks were largely along $\langle 1\bar{1}2 \rangle$ directions confirming the results of Puttick and Hosseini (128) with smaller $\langle 1\bar{1}0 \rangle$ cracks also occurring. Details of the variation of radial and lateral crack lengths with temperature and applied load are given below, along with data for all the other materials investigated.

Figures 10, 11 and 12 show the variation of radial crack radius (c_r) with temperature and applied load for SiC, Si_3N_4 and {111} single crystal Si respectively. Generally, all the materials showed some increase in c_r with increasing temperature at each load, the form of the curve being either linear (Carborundum sintered SiC, PDSN, RBSN, NCX34 hot-pressed Si_3N_4 , {111} Si above 300°C) or curved with a high-temperature plateau (NC203 hot-pressed SiC, Suzuki sintered SiC, NC132 hot-pressed Si_3N_4). Whilst most materials showed a substantial ($\sim 50\%$) increase in crack lengths over the temperature range, both RBSN (fig. 11b) and, especially, NC132 hot-pressed Si_3N_4 (fig. 11c) displayed very little variation. The temperature sensitivity of radial crack extent was particularly interesting

in the case of {111} single crystal Si, which showed no change in c_r up to $\sim 300-400^\circ\text{C}$, followed by a marked linear increase up to 700°C , above which no radial cracking was observed. In this case, the variation of lateral crack extent c_ℓ (for lateral cracks seen to emerge at the surface only) was also measured for 1 kgf indentations. Despite the relatively large statistical spread in results, c_ℓ was observed to peak at $\sim 200^\circ\text{C}$ with $c_\ell \approx c_r$, and then to die away with increasing temperature, such that above 300°C surface lateral cracks were rare.

The ratio (c/a) of radial crack extent to indentation radius was calculated for 1 kgf indentations for each material/temperature (table 4). With the exception of the single crystal silicon, this parameter was remarkably constant as a function of temperature for each material, indicating that c_r increased with temperature in direct proportion to a (at constant load). (c/a) varied from ~ 1.6 (NC132) to ~ 4.3 (single crystal SiC at 800°C). Single crystal silicon had a maximum (c/a) value of 4.1 at 500°C , decreasing to zero at 800°C .

Using data from table 3, the ratio (c/b) of radial crack radius to plastic zone radius was calculated, again for a constant applied load of 1 kgf. Radial cracks generally extended significantly beyond the calculated plastic zone for the most brittle materials examined (single crystal SiC, Carborundum sintered SiC, PDSN) whilst, for other materials, radial cracks were contained wholly within the calculated plastic zone. For SiC and Si materials, (c/b) decreased with increasing temperature (i.e. b increased more rapidly than c), this being most evident for the single crystal silicon above 500°C . The silicon nitride specimens showed very little change in (c/b) with temperature.

The effect of including a plastic zone radius term in the calculation of K_{IC} (equation d) is demonstrated in figure 13 in the case of hot-pressed SiC. Without this term, the calculated values of K_{IC} decrease with increasing temperature, reflecting the variations of c_r , as reported earlier (1). Including the term results in lower calculated values for K_{IC} , the temperature variations (table 6) being eliminated (fig. 13, lower curve) - the implications of this are discussed in section 6.2.1.

Indentation fracture toughness values calculated according to equation d are presented in table 6 for all materials/temperatures. Each material showed a $Pac^{3/2}$ relationship except NCX34 hot-pressed Si_3N_4 , where the exponent increased with temperature from ~ 1.7 at 22°C to ~ 2.6 at 800°C ! This renders the K_{IC} values calculated for NCX34 meaningless, although they appear reasonable in magnitude. As with hot-pressed SiC, the majority of materials showed no variation of K_{IC} with temperature within the limits of experimental error, save in the following cases: (0001) single crystal Si showed a decrease in K_{IC} from 1.7 MPam $^{3/2}$ at room temperature to 1.0 MPam $^{3/2}$ at 800°C , 'Suzuki' sintered SiC had an anomalously high value of K_{IC} at room temperature and PDSN perhaps showed a small decrease in K_{IC} with temperature. The dependence of K_{IC} on microstructure is described and discussed in section 6.2.1.

Finally, the 'index of brittleness (H/K_{IC}) ' defined by Lawn and Marshall (123) has been plotted against temperature for SiC (fig. 14), Si_3N_4 (fig. 15) and Si (fig. 16) materials. By this classification, Si is the most 'brittle' of the materials studied (at low temperatures),

the index of brittleness decreasing rapidly with increasing temperature. SiC materials were generally more 'brittle' than Si₃N₄ specimens (except PDSN) and again showed a decrease in (H/K_{IC}) with temperature (not as pronounced as in Si). The nitrides all showed very little, if any, change in 'brittleness' with temperature.

5.2.2. CRACK INITIATION

The critical load required for crack nucleation P^* , has been plotted as a function of temperature for each material (figs. 17-19). In calculating P^* , the coefficient λ_0 in equation e was taken to be 9×10^4 so as to yield values in approximate agreement with observed values of limiting loads for radial crack development. For example, RBSN formed little or no radial fracture below 500 gf ($\sim 5N$) over the whole temperature range; NC132 behaved similarly up to 200°C, above which no radial cracks formed at loads below 1 kgf ($\sim 10N$). {111} single crystal silicon showed the following 'cut-off' loads: 200 gf ($\sim 2N$) at 500°C, 500 gf ($\sim 5N$) at 600°C and 1 kgf ($\sim 10N$) at 700°C, where relatively few cracks formed (although those that did were more extensive than radial cracks formed at 600°C, as described in the previous section). Choosing $\lambda_0 = 9 \times 10^4$, P^* values calculated from equation e were consistent with these estimates to within at least an order of magnitude, often much better. This is reasonable, considering that typical experimental errors (not shown in figs. 17-19) were of the order of 60% due to the dependence on high powers of K_{IC} and H (10% error in K_{IC} and 5% error in H would result in a possible 55% error in P^*).

Despite the inaccuracy of absolute values, a clear idea of both the temperature and microstructural variations of P^* may be obtained from figs. 17-19. (NB a logarithmic scale has been used for these plots since P^* changed by two or even three orders of magnitude in some cases). Generally, both SiC and Si₃N₄ materials showed no change in P^* with temperature up to ~ 300 -400°C, whilst at higher temperatures many materials exhibited an increase in P^* with increasing temperature. This increase was dramatic (2 orders of magnitude) in the case of PDSN but less pronounced (half an order of magnitude) for sintered and hot-pressed carbides and for NC132 hot-pressed Si₃N₄. Single crystal SiC, NCX34 hot-pressed Si₃N₄* and RBSN showed no change in P^* with temperature at all. For single crystal Si (fig.19), P^* increased by three orders of magnitude between room temperature and 700°C, the increase being most pronounced above 500°C. Microstructural factors are discussed in section 6.2.2.

* K_{IC} values for this material were unreliable, however, as described in the previous section.

6. DISCUSSION

6.1. HARDNESS AS A FUNCTION OF TEMPERATURE

Possible mechanisms for the decrease in hardness with increasing temperature have been reviewed in section 2.3. In summary, the effect may be due to any of the following:

- i) diminution of the CRSS for dislocation glide (this may involve a decrease in the Peierls stress or increased diffusion of pinning mechanisms, and is almost certainly a function of dislocation character);
- ii) a change in active slip systems (single crystal hardness anisotropy measurements at various temperatures indicate that this is unlikely in SiC (105) and Si₃N₄ (107);
- iii) thermally activated cross slip and climb effects (30);
- iv) movement of double kinks by phonon-assisted electron tunnelling (35, 36);
- v) the increased contribution of grain boundary sliding at high temperatures for polycrystalline materials.

Mechanisms such as twinning, deformation-induced phase transformations and block shear are likely to be athermal in nature.

In general, SiC materials showed a marked (~60%) decrease in hardness over the temperature range 0.1-0.35 T_m, whilst Si₃N₄ showed a ~30% decrease over a larger homologous temperature range (0.15 - 0.5 T_m). Thus, the room temperature hardness superiority of SiC over most forms of Si₃N₄ is not maintained at high temperatures (~600°C). Neither material showed a knee in the hardness/temperature curves in these temperature ranges, although the Knoop hardness data for SiC presented earlier (1) often showed athermal regions extending up to ~100-200°C. The SiC data is thus not consistent with Gilman's electron tunnelling theories (35, 36), which predict a knee in the curve at approximately the Debye temperature, which is 930°C for α-SiC and 1200°C for β-SiC (135). (As yet, no value of θ_D for Si₃N₄ has been found in the literature). Evidence of gross plasticity, in the form of surface slip steps, was not found in SiC below ~800°C (1, 105), and slip steps were not observed at all in Si₃N₄, except possibly in one anomalously large grain of RBSN at 800°C (fig. 6c). It is clear that direct observations of deformation structures around indentations made at various temperatures will be required to explain the hardness/temperature variations reported here.

Microstructural effects are difficult to assess in these materials, since the variables (e.g. porosity and grain size) are not generally independent of each other. Broadly, microstructure had a much more pronounced effect on the hardness/temperature curves for Si₃N₄ materials than for silicon carbides (figs. 1 and 2).

Of the SiC materials, the (0001) single crystal was consistently the hardest, even though this crystal orientation has been reported to show comparatively low hardness values (e.g. 13). For instance, the Knoop hardness of a {10 $\bar{1}$ 0} plane with the long indenter axis

approximately 30° from a $\langle 11\bar{2}0 \rangle$ direction has been found to be $\sim 25\%$ greater than on the (0001) plane with indenter axis along $\langle 11\bar{2}0 \rangle$ (as used here)*. Thus the high hardness value for the single crystal is not just caused by an unfavourably oriented slip system, as speculated earlier (1) - indeed, it appears that grain boundaries have a definite softening effect, perhaps due to stress-activated boundary sliding (this hypothesis is advanced tentatively).

With the exception of the reaction-bonded material, and possibly the single crystal (where more data points are required to determine the precise form of the H/T curve) the slopes of the log (hardness) vs temperature graphs were identical, suggesting a common deformation process for these materials. The relative softness of 'Suzuki' sintered SiC in comparison with hot-pressed and Carborundum sintered materials may have been due to the extra porosity in this sample (see section 2.3). The form of the curve for REFEL reaction-bonded SiC seems to be partly due to the $\sim 12\%$ residual Si content in this material: correcting for this using the hot-hardness data obtained for {111} Si results in a hardness/temperature curve very similar to that of the 'Suzuki' sintered SiC.

Figure 2a (same scale as fig.1a) shows that microstructural effects are much more important in silicon nitride materials. The hardest form of Si_3N_4 examined was the relatively coarse-grained ($\sim 50\mu\text{m}$) PDSN, thus confirming the softening effect of grain boundaries. The principle difference between NC132 and NCX34 hot-pressed nitrides (curves 3 and 4, figure 2) lies in the pressing additive used, and hence the boundary phase (section 2.3), and the constant offset in the two curves must reflect this difference (it is a real effect, not simply due to the volume fraction of softer material introduced). Although Y_2O_3 is known to reduce the amount of boundary sliding observed in high-temperature creep processes (63), it is present as a thicker boundary layer than in the MgO-pressed material (figs. 7 and 8). The relative hardness behaviour of these two materials at higher temperatures will be of considerable interest.

The RBSN sample showed little variation of hardness with temperature, the low-temperature hardness being suppressed by comparison with the hardness/temperature curves for the hot-pressed materials. This is likely to be caused by compaction effects due to the $\sim 13\%$ porosity present in this specimen - porosity effects are reviewed in section 2.3.

The variation of the calculated (124) ratio (b/a) of plastic zone size to indentation radius with temperature is shown in table 3. Although surface plasticity effects (e.g. slip steps) are not observed to extend far beyond the indentation profile at low temperatures, the depth to which the deformed zone extends beneath an indentation has rarely been determined (see section 2.2). Lankford and Davidson (82) have estimated (b/a) ~ 5.5 in 4H single crystal SiC by selected area electron channelling methods, whilst Hockey et al. (7) have measured the near-surface (b/a) ratio to be ~ 2 by TEM observations. These values compare with the calculated value of (b/a) ~ 2.33 at room temperature (table 3).

* Of course, the anisotropy in Vickers hardness will be less than that in the Knoop case.

The shape of the plastic zone is unlikely to be precisely spherical (82), however, so care must be taken in defining a plastic zone size parameter. The ratio (b/a) is important in deriving K_{IC} values from radial crack measurements, as described in section 3.1.

6.2. INDENTATION FRACTURE

6.2.1. CRACK PROPAGATION

Radial cracks were generally found to become more extensive with increasing temperature; this effect was material-dependent, being most pronounced for $\{111\}$ Si (above 300°C), rather less marked for SiC materials, the Si_3N_4 specimens showing comparatively little change in crack lengths with temperature. The reasons for the two forms of c_r /temperature curve (linear and curved with high-temperature plateau) remain unclear - there seems no consistent microstructural similarity between materials showing the same type of behaviour. The temperature sensitivity of surface lateral crack extent in $\{111\}$ Si is both interesting and unexpected: Evans and Wilshaw (116) have observed that the ratio of radial to lateral crack extents is often proportional to a factor $(PH/K_{IC}^2)^{1/4}$ which increases with applied load, but decreases with increasing temperature. Since only the lateral cracks which broke through to the surface could be measured, it is possible that the effect was related to a change in lateral crack depth as well as extent.

The relative insensitivity of the ratio (c/a) to temperature may be explained in terms of the Lawn et al. theory (124), since this predicts $(c/a)\propto H^{1/6}$ (for constant load and assuming K_{IC} to be temperature-insensitive), a relatively weak function of temperature. The calculated ratio (c/b) (table 5) indicates that several materials may form cracks wholly within the plastic zone at 1 kgf load, even at room temperature, and this leads to speculation concerning the extent to which crack propagation depends on plasticity (discussed in reference 46). In particular, $\{111\}$ Si has been speculated to form $\langle\bar{1}\bar{1}2\rangle$ radial cracks (as observed here) by dislocation interaction (137). Less extensive cracking along $\langle\bar{1}\bar{1}0\rangle$ directions was also observed in the current investigation, and this argues against preferential fracture along planar slip bands, as observed in some metal alloys (47). Whether plasticity is important in crack propagation or not, the relationship $Pac^{3/2}$ (124) was observed in all materials save one (NCX34 hot-pressed Si_3N_4), regardless of (c/b) ratio.

The reasons for the strange behaviour of NCX34 silicon nitride remain unclear, the coefficient m in the relation $c\propto P^m$ decreasing progressively from 0.59 at room temperature to 0.38 at 800°C (corresponding to either enhanced low-load cracking or suppressed high-load fracture). As discussed in the previous section, the principle difference between NCX34 and NC132 (which showed normal behaviour) hot-pressed nitrides is likely to be in grain boundary structure, and it is suggested that some progressively thermally-activated boundary mechanism may be responsible for this behaviour. Clearly, further work is required to elucidate this matter.

K_{IC} values were calculated according to equation d (figure 13 shows the effect of the plastic zone size term c.f. earlier theories (eg 123)).

As discussed in section 3.1, the residual stress due to the plastic zone provides the driving force for radial crack extension, and as the temperature is increased the plastic zone becomes larger, resulting in longer cracks. The K_{IC} values derived (table 6) were, to within experimental errors, largely temperature-insensitive, confirming bulk mechanical measurements in the same temperature range (e.g. 133).

Comparing absolute values with those obtained from the literature (table 1), shows that values for Si and NC132 hot-pressed silicon nitride are in reasonable agreement, but values obtained for SiC materials are a factor of 1-4 less than those obtained by other methods. Possible explanations for this could include:-

- (1) the plastic zone may be larger than predicted by the simple model assumed in equation d (see section 3.1), resulting in larger crack sizes than expected, hence lower K_{IC} values,
- (2) a similar effect would be measured if substantial slow crack growth were to take place between indentation and measurement (this is currently under investigation).
- (3) finally, effects due to Poisson's ratio and indenter friction have been discussed, but not quantified, by Evans (70). In particular, indentation fracture theories often assume $\nu=0.25$ as observed in silicon and silicon nitride (table 1), however Poisson's ratio is generally substantially lower (0.15 - 0.2) in SiC materials.

Despite these uncertainties, certain general trends emerge from table 6 - for instance, hot-pressed materials have relatively high values of K_{IC} , whilst single crystals and coarse-grained materials have low values, as do porous materials. Microstructural effects on K_{IC} have been discussed by several authors (e.g. 25, 65, 109, 133, 137-145), and some relevant points are summarized below.

As mentioned in section 4.1, all the hot-pressed materials were observed to contain small W-rich inclusions at the boundaries, and such inclusions are thought to interact with cracks and result in higher K_{IC} values (e.g. 65, 137, 138), although this effect will generally depend on the nature of the particles (137,139). At high temperatures, e.g. above 1200°C for hot-pressed Si_3N_4 (140), slow crack growth may dominate the fracture behaviour, depending on impurity and grain size (e.g. 141).

Crack paths in single crystals and large-grained materials were generally straighter over much of their lengths than in fine-grained materials, where cracks often passed preferentially along grain boundaries, giving rise to a 'meandering' appearance. This latter effect presumably results in more difficult crack propagation, hence higher K_{IC} . A corresponding effect is observed in large-scale fracture tests, where the ratio of transgranular to intergranular cleavage is more important than grain size (although the two may be related) and grain boundary cohesion is an important parameter (137). Grain shape has also been found to be important in hot-pressed silicon nitrides (e.g. 142-144): more elongated grains resulting in higher toughness.

Finally, porosity is an important factor in determining materials' toughness: detrimental effects include stress concentration (pore size

and shape being important) and boundary weakening (if intergranular), whilst beneficial effects may arise from interactions resulting in crack deflection or crack arrest (e.g. 138, 145). Although this latter effect was observed in many materials in the present study, the overall effect (table 6) of porosity appears to have been detrimental in most cases.

Lawn et al. (e.g. 123) have defined an 'index of brittleness' (H/K_{IC}) (a generalized, but equivalent treatment is given by Puttick (126)), which has been plotted as a function of temperature for each material (figs. 14-16). Whilst Si showed a strong decrease in 'brittleness' with increasing temperature, SiC materials showed a smaller decrease, and Si_3N_4 materials very little variation at all. Thus, SiC materials are generally more brittle than Si_3N_4 ceramics until high temperatures ($\sim 800^\circ\text{C}$) are reached. The index of brittleness is thought to be an important parameter for materials selection for abrasive environments in the fracture-controlled régime (123).

6.2.2. CRACK INITIATION

As mentioned in section 3.2, temperature effects on crack nucleation parameters are difficult to predict but, using the parameter $P^* \propto (K_{IC}^4/H^3)$, may be easily compared. The form of the above relationship is believed to be generally valid (it may be derived dimensionally), but the coefficient of proportionality (λ_0) depends on the process responsible for crack nucleation (e.g. sampling of pre-existing flaws (122) or slip band interpenetration (45) or blocking of glide bands by grain boundaries (41-43) or boundary cavitation (81)). Thus, a better approach might be to measure P^* directly and derive λ_0 values for a range of materials in order to assess which mechanisms operate as a function of material/microstructure/temperature etc. In this investigation, a value of $\lambda_0 \sim 9 \times 10^4$ (c.f. 1.6×10^4 (123)) was found to give reasonable agreement with the limited number of P^* values observed directly.

Crack nucleation was generally observed to become more difficult at high temperatures, and this is reflected in many of the P^* versus temperature curves in figs. 17-19. The effect was most pronounced in the case of {111} Si, the curve showing a sudden up-turn at around $500-600^\circ\text{C}$, the temperature range above which surface slip steps were observed to form. If slip band interpenetration is responsible for crack nucleation in this material, high temperatures may cause a decrease in stress concentration (due to slip band widening, etc.) or may enable dislocation climb to occur, both of which would be consistent with more difficult crack nucleation.

The most obvious microstructural effect on P^* is that of grain size, coarse-grained materials and single crystals showing relatively easy nucleation. This is consistent with equation (g) setting D equal to the grain size (i.e. having the possibility of large dislocation pile-ups creating stress concentration). Porosity seems to decrease both H (at low temperatures) and K_{IC} , and from figs. 17 and 19 appears to have relatively little effect on P^* , at least for the materials investigated.

However, despite these generalisations, a full understanding of the role of crack nucleation in indentation fracture must await detailed explanations of the possible micro-mechanics of crack genesis in a variety of materials.

7. CONCLUSIONS

Temperature - and load-variable microhardness tests have been used to study the changing incidence of plasticity and fracture in SiC, Si₃N₄ and Si materials as a function of specimen microstructure.

The decrease of hardness with temperature was more marked for SiC than for Si₃N₄ materials, such that the room temperature superiority of SiC over most forms of Si₃N₄ (only PDSN, has comparable room temperature hardness) was not maintained above $\sim 600^{\circ}\text{C}$. The hardness/temperature curve for {111} single crystal Si was similar in form to those reported by previous workers.

Microstructural influences on hardness were more pronounced in Si₃N₄ than in SiC. Grain boundaries were generally observed to cause softening, and often provided preferred fracture paths, especially in fine-grained materials and especially at high temperature (800°C). However, K_{IC} values were highest for fine-grained materials, probably due to crack deflection by grain boundaries.

Porosity was found to produce a decrease in hardness, especially at low temperatures, and provided crack termination sites and preferred fracture paths in some cases.

Cracking (radial and/or lateral) became more severe with increasing temperature, presumably due to an increase in crack-opening force provided by the concomitant increase in plastic zone size. The effect was most marked for {111} single crystal Si, followed by SiC materials, the Si₃N₄ specimens showing relatively little change in crack extent with temperature. Crack nucleation became more difficult with increasing temperature.

K_{IC} values were derived using a recently-published theory (124), and were found to be independent of temperature up to 800°C , agreeing with bulk mechanical values in the case of Si and Si₃N₄, values for SiC being somewhat lower than those reported in the literature.

Finally, hardness was found to be slightly dependent on applied load (between 0.1 and 1 kgf), insensitive to impurity in certain doped Si and SiC materials, and sensitive to surface finish where polishing damage was apparent optically.

The results are of direct relevance to both abrasion and (probably) erosion processes, indentation results being more useful than bulk mechanical properties as guides for materials selection for surface-contact applications.

8. FURTHER WORK

The following experiments are considered crucial in further understanding the effects of temperature on surface contact phenomena in SiC and Si₃N₄ materials:

- TEM examination of deformation mechanisms operating beneath indentations/scratches for comparison with those already studied at room temperature (e.g. 9);
- determination of single crystal SiC hardness anisotropy as a function of temperature, in order to identify the active slip systems at each point on the hardness/temperature plot;
- investigation of indentation creep effects, at temperatures up to 1200°C;
- investigation of possible chemomechanical effects;
- measurement of coefficients of friction in simple sliding stylus experiments.

9. ACKNOWLEDGEMENTS

The European Research Office of the U.S. Army is gratefully acknowledged for support and sponsorship. Thanks are also due to Prof. R.W.K. Honeycombe for the provision of laboratory facilities, and to SRC for funding of the hot-hardness tester. We would also like to thank Dr. R.N. Katz (AMMRC, Watertown, USA), Mr. P. Kennedy, (UKAEA, Springfields), Dr. D.J. Godfrey (Admiralty Marine Technology Establishment, Holton Heath) and Texas Instruments (U.K.) Ltd., for supplies of specimen material. Messrs. M. Stocker, B. Barber and Ms. V. Kohler are gratefully acknowledged for technical assistance, as is Dr. K. Gove for advice and co-operation concerning the construction of the hot-hardness tester. Finally, thanks are due to Mrs. E. Palmer for typing the manuscript.

25.

10. REFERENCES

1. M.G.S. Naylor and T.F. Page, 1979, Technical Report to U.S. Army, October 1979, Contract No. DAERO-78-G-010.
2. J.J. Burke, A.E. Gorum and R.N. Katz, 1974, "Ceramics for High Performance Applications" (Army Materials Technology Conference Series), Brook Hill.
3. R.N. Katz, 1980, Proceedings of the Third International Conference on Mechanical Behaviour of Materials, 20th August 1979, Volume 1, Eds. K.J. Miller and R.F. Smith, Pergamon Press.
4. P. Kennedy and J.V. Shennan, 1973, Atom (No. 206), 260.
5. "Silicon Nitride as a Bearing Material", Program Review: U.S. Naval Air Systems Command and U.S. Office of Naval Research, July 1974. (Proc. of a meeting held at SKF, King of Prussia, Pa. 9-10 July, 1974).
6. J.W. Edington, D.J. Rowcliffe and J.L. Henshall, 1975, Powder Met. Int. 7, No. 3, 136.
7. B.J. Hockey and S.M. Wiederhorn, 1979, Proceedings of the Fifth International Conference on Erosion by Liquid and Solid Impact (ELSI V), 3-6th September 1979, Newnham College, Cambridge. Publ. R.A.E. Farnborough. p.26.
8. A.G. Evans, M.E. Gulden and M. Rosenblatt, 1978, Proc. Roy. Soc. Lond. A361, 343.
9. T.F. Page, G.R. Sawyer, O.O. Adewoye and J.J. Wert, 1978, Proc. Brit. Ceram. Soc. 26, 193.
10. O.O. Adewoye, 1976, Ph.D. thesis, University of Cambridge.
11. G.R. Sawyer, 1979, Ph.D. thesis, University of Cambridge.
12. G.R. Sawyer and T.F. Page, 1978, J. Mater. Sci. 13, 885.
13. G.R. Sawyer, P.M. Sargent and T.F. Page, 1980, J. Mater. Sci. 15, 1001.
14. O.O. Adewoye and T.F. Page, 1976, J. Mater. Sci. 11, 981.
15. P.M. Sargent, 1979, Ph.D. thesis, University of Cambridge.
16. P.M. Sargent and T.F. Page, 1978, Proc. Brit. Ceram. Soc. 26, 209.
17. N.W. Jepps and T.F. Page, 1979, J. Microscopy, 116, 159.
18. M.G.S. Naylor, 1978, M. Phil thesis, University of Cambridge, Department of Metallurgy and Materials Science.
19. M.G.S. Naylor and T.F. Page, 1979, as reference 7, p.32.
20. O.O. Adewoye, G.R. Sawyer, J.W. Edington and T.F. Page, 1974, Technical Report to U.S. Army (AMMRC), October 1974, Contract No. DAJA-74-C-1310.

21. R.C. Bradt and R.E. Tressler, (Eds.), 1974, "Deformation of Ceramic Materials", Proceedings of a symposium held at Penn. State University, July 17-19, 1974 (Plenum Press).
22. R.M. Latanision and J.T. Fourie (Eds.), 1977, "Surface Effects in Crystal Plasticity", Nato Advanced Study Inst. Series (Nordhoff, Leyden).
23. A. Kelly, 1966, "Strong Solids", Clarendon Press, Oxford.
24. P.C. Dokko and J.A. Pask, 1976, Mater. Sci. Eng. 25, 77.
25. J.W. Edington, D.J. Rowcliffe and J.L. Henshall, 1975, Powder Met. Int. 7, No. 2, 82.
26. A.G. Evans and J.V. Sharp, 1971, J. Mater. Sci. 6, 1292.
27. A.R. Verma and P. Krishna, 1966, "Polymorphism and Polytypism in Crystals", J. Wiley Inc., p.93.
28. D.J. Smith, N.W. Jepps and T.F. Page, 1978. J. Microscopy 114, 1.
29. R. von Mises, 1928, Z. Angew. Math. Mech. 8, 161.
30. G.W. Groves and A. Kelly, 1963, Phil. Mag. 8, 877.
31. H.L. Fotedar and T.G. Stoebe, 1975, Phys. Stat. Sol. (a) 31, 399.
32. M. Srinivasan and T.G. Stoebe, 1974, J. Mater. Sci. 9, 121.
33. A.G. Evans and T.G. Langdon, 1976, Progress in Materials Science 21, 214.
34. P.B. Hirsch, 1980, J. Microscopy 118, 3.
35. J.J. Gilman, 1968, J. Appl. Phys. 39, 6086.
36. J.J. Gilman, 1975, J. Appl. Phys. 46, 5110.
37. C.H. Woo and M.P. Puls, 1977, Phil. Mag. 35, 1641.
38. H.L. Fotedar and T.G. Stoebe, 1971, Phil. Mag. 23, 859.
39. M. Srinivasan and T.G. Stoebe, 1970, J. Appl. Phys. 41, 3726.
40. R.W. Davidge and A.G. Evans, 1970, Mater. Sci. Eng. 6, 281.
41. A.R.C. Westwood, 1961, Phil. Mag. 6, 195.
42. R.C. Ku and T.L. Johnston, 1964, Phil. Mag. 9, 231.
43. J. Moriyoshi, W.D. Kingery and J.B. Van der Sande, 1977, J. Mater. Sci. 12, 1062.
44. J.T. Hagan, M.V. Swain and J.E. Field, 1979, in "The Science of Ceramic Machining and Surface Finishing II", Eds. B.J. Hockey and R.W. Rice, National Bureau of Standards Special Publication 562 (U.S. Government Printing Office, Washington, D.C.) p.15.

27.

45. J.T. Hagan, 1979, J. Mater. Sci. 14, 2975.
46. B.R. Lawn, R.J. Hockey and S.M. Wiederhorn, 1980, J. Mater. Sci. 15, 1207.
47. D.A. Koss and K.S. Chan, 1980, Acta. Metall. 28, 1245.
48. A.H. Heuer, 1970, Proc. Brit. Ceram. Soc. 15, 173.
49. V.G. Eremenko and V.I. Nikitenko, 1972, Phys. Stat. Sol. (a) 14, 317.
50. W.D. Kingery, 1974, J. Am. Ceram. Soc. 57, 1.
51. P. Chaudhari and J.W. Matthews, 1971, J. Appl. Phys. 42, 3063.
52. D.R. Clarke and G. Thomas, 1977, J. Am. Ceram. Soc. 60, 491.
53. A.H. Heuer, V. Lou, L. Ogbuji and T.E. Mitchell, 1977, J. Microsc. Spectrosc. Electron, 2, 475.
54. D.R. Clarke and G. Thomas, 1978, J. Am. Ceram. Soc. 61, 114.
55. L.K.V. Lou, T.E. Mitchell and A.H. Heuer, 1978, *ibid.*, 61, 392.
56. P. Drew and M.H. Lewis, 1974, J. Mater. Sci. 9, 261.
57. O. Krivanek, T.M. Shaw and G. Thomas, 1979, J. Am. Ceram. Soc. 62, 585.
58. B.S.B. Karunaratne and M.H. Lewis, 1980, J. Mater. Sci. 15, 1781.
59. H. Foll and D. Ast, 1979, Phil. Mag. A. 40, 589.
60. C. Fontaine and A. Rocher, 1980, J. Microscopy 118, 105.
61. A.G. Evans and A. Rana, 1980, Acta. Metall. 28, 129.
62. P.L. Farnsworth and R.L. Coble, 1965, J. Am. Ceram. Soc. 49, 264.
63. G.E. Gazza, 1975, Bull. Am. Ceram. Soc. 54, 778.
64. A.G. Evans and S.M. Wiederhorn, 1974, J. Mater. Sci. 9, 270.
65. R.L. Tsai and R. Raj, 1980, J. Am. Ceram. Soc. 63, 513.
66. R.B. Day and R.J. Stokes, 1966, *ibid.* 49, 345.
67. M.N. Sinha, D.J. Lloyd and K. Tangri, 1973, J. Mater. Sci. 8, 116.
68. B.R. Lawn and T.R. Wilshaw, 1975, *ibid.* 10, 1049.
69. R. Hill, 1950, "The Mathematical Theory of Plasticity", (Clarendon Press, Oxford).
70. A.G. Evans, 1980, Am. Soc. Test. Mater. Spec. Tech. Publ., No. 678.
71. B.J. Hockey and B.R. Lawn, 1975, J. Mater. Sci. 10, 1275.

72. B.J. Hockey, S.M. Wiederhorn and H. Johnson, 1978, "Fracture Mechanics of Ceramics", Vol. 3, (Eds. R.C. Bradt, D.P.H. Hasselman and F.F. Lange), Plenum-Press, p.379.
73. B.J. Hockey, 1971 J. Am. Ceram. Soc. 54, 223.
74. R. Stickler and G.R. Booker, 1962, Phil. Mag. 8, 859.
75. M.J. Hill and D.J. Rowcliffe, 1974, J. Mater. Sci. 9, 1569.
76. M. Kitada, 1980, ibid. 15, 1684.
77. M.A. Velednitskaya, V.N. Rozhanskii, L.F. Comolova, G.V. Saparin, J. Schreiber and O. Brümmer, 1975, Phys. Stat. Sol. 32, 123.
78. S.M. Hu, 1975, J. Appl. Phys. 46, 1470.
79. C.A. Brookes and M.P. Shaw, 1976, Nature 263, 760.
80. C.A. Brookes, 1977, "Surface Effects in Crystal Plasticity" (Eds. R.M. Latanision, and J.T. Fourie), Nato Advanced Study Inst. Series (Nordhoff, Leyden), p.671.
81. S. Van der Zwaag, J.T. Hagan and J.E. Field, 1980, J. Mater. Sci. 15, 2965.
82. J. Lankford and D.L. Davidson, 1979, ibid. 14, 1669.
83. C.A. Brookes, J.B. O'Neill and B.A.W. Redfern, 1971, Proc. Roy. Soc. Lond. A322, 73.
84. B. Subramaniam and K.G. Bansigir, 1980, J. Mater. Sci. 15, 2889.
85. B.J. Busovne, Jr., D.M. Kotchick and R.E. Tressler, 1979, Phil. Mag. A. 39, 265.
86. I.V. Gridneva, Yu.V. Milman, and V.I. Trefilov, 1972, Phys. Stat. Sol. 14, 177.
87. V.I. Trefilov, V.A. Borisenko, G.G. Gnesin, I.V. Gridneva and Yu. V. Milman, 1977, Dokl. Akad. Nauk. SSSR 239, 579 (in Russian).
88. A.G. Atkins and D. Tabor, 1966, Proc. Roy. Soc. Lond. A292, 441.
89. A.G. Atkins, 1971, "The Science of Hardness Testing and its Research Applications" (Eds. J.H. Westbrook and H. Conrad), American Society for Metals, p.223.
90. J.H. Westbrook, 1957, Proc. Amer. Soc. Test. Mats. 57, 873.
91. H.D. Merchant, G.S. Murty, S.N. Bahadur and Y. Mehrotra, 1973, J. Mater. Sci. 8, 437.
92. J.J. Gilman, 1971, as reference 89, p.51.
93. K. Ito, 1923, Tohoku Sci. Repts. 12, 137.
94. V.P. Shishokin, 1930, Z. Physik. Chem. 189, 263.
95. V.I. Trefilov and Yu. V. Milman, 1963, Soviet Physics Doklady 8, 1240.

96. A.G. Atkins, A. Silvério and D. Tabor, 1966, J. Inst. Metals 94, 369.
97. L.M. Fitzgerald, 1963, J. Less-Common Metals. 5, 356.
98. R.D. Koester and D.P. Moak, 1967, J. Am. Ceram. Soc. 50, 290.
99. Y. Kumashiro, A. Itoh, T. Kinoshita and M. Sobajima, 1977, J. Mater. Sci. 12, 595.
100. Y. Kumashiro and E. Sakuma, 1980, *ibid.* 15, 1321.
101. R.H.J. Hannink, D.L. Kohlstedt and M.J. Murray, 1972, Proc. Roy. Soc. Lond. A326, 409.
102. D.L. Kohlstedt, 1973, J. Mater. Sci. 8, 777.
103. D.J. Rowcliffe and G.E. Hollox, 1971, *ibid.* 6, 1261.
104. *Idem*, *ibid.*, 6, 1270.
105. T. Hirai and K. Niihara, 1979, *ibid.* 14, 2253.
106. T.N. Loladze, G.V. Bokuchava and G.E. Davidova, 1971, as reference 89, p.251.
107. K. Niihara and T. Hirai, 1979, J. Mater. Sci. 14, 1952.
108. I.C. Huseby and G. Petzow, 1974, Powder Met. Int. 6, 17.
109. R.W. Rice, 1977, Treatise on Materials Science and Technology II, Ed. R.K. MacCrone, Academic Press, p.199.
110. A.R.C. Westwood, D.L. Goldheim and R.G. Lye, 1967, Phil. Mag. 16, 505.
111. N.H. MacMillan, 1977, as reference 80, p.629.
112. A.R.C. Westwood and N.H. MacMillan, as reference 89. p.377.
113. C.A. Brookes and A.G. Atkins, 1964, Proc. 5th. Plansée Seminar, Reutte 1964, Springer-Verlag 1965, p.712.
114. B.R. Lawn and M.V. Swain, 1975, J. Mater. Sci. 10, 113.
115. B.R. Lawn and E.R. Fuller, 1975, *ibid.* 10, 2016.
116. A.G. Evans and T.R. Wilshaw, 1976, Acta. Metall. 24, 939.
117. M.V. Swain and J.T. Hagan, 1976, J. Phys. D. 9, 2201.
118. J.T. Hagan, 1979, J. Mater. Sci. 14, 462.
119. C.M. Perrott, 1977, Wear 45, 293.
120. M.A. Moore, 1979, Proc. Int. Conf. "Wear of Materials", Dearborn, Michigan, April 16-18, 1979 (Eds. K.C. Luderna, W.A. Glaeser and S.K. Rhee), p.275.
121. B.R. Lawn, T. Jensen and A. Arora, 1976, J. Mater. Sci. 11, 573.

122. B.R. Lawn and A.G. Eyans, 1977, *ibid.* 12, 2195.
123. B.R. Lawn and D.B. Marshall, 1979, *J. Am. Ceram. Soc.* 62, 347.
124. B.R. Lawn, A.G. Evans and D.B. Marshall, 1980, *ibid.* 63, 574.
125. B.R. Lawn and D.B. Marshall, 1979, *ibid.* 62, 106.
126. H.P. Kirchner and R.M. Gruver, 1978, as reference 72, p.365.
127. C.T. Peters, 1979, *J. Mater. Sci.* 14, 1619.
128. K.E. Puttick and M.M. Hosseini, 1980, *J. Phys. D.* 13, 875.
129. J.T. Hagan, 1980, *J. Mater. Sci.* 15, 1417.
130. H. Suzuki, 1980, private communication.
131. K.C. Pitman and D.J. Godfrey, 1978, *Proc. Brit. Ceram. Soc.* 26, 225.
132. G.D. Quinn, 1980, Technical report to U.S. Department of Energy by AMMRC, Interagency Agreement EC-76-A-1017.
133. J.L. Henshall, 1975, Ph.D. thesis, University of Cambridge.
134. C.P. Chen and H. Leipold, 1980, *Bull. Am. Ceram. Soc.* 59, 469.
135. R.C. Marshall, J.W. Faust, Jr. and C.E. Ryan, (Eds.), 1973, *Silicon Carbide - 1973. Proc. 3rd. Int. Conf. on SiC*, Florida, University of South Carolina Press, p.668.
136. D. Chakraborty and J. Mukerji, 1980, *J. Mater. Sci.* 15, 3051.
137. J.D.B. Veldkamp and N. Hattu, 1979, *Phillips Journal of Research*, 34, 1.
138. C.T. Forwood and A.J. Forty, 1965, *Phil. Mag.* 11, 1067.
139. C. Greskovich and J.A. Palm, 1980, *J. Am. Ceram. Soc.* 63, 597.
140. R.K. Govila, K.R. Kinsman and P. Beardmore, 1979, *J. Mater. Sci.* 14, 1095.
141. B.J. Dalgleish, A. Fakhr, P.L. Pratt and R.D. Rawlings, 1979, *ibid.*, 2605.
142. F.F. Lange, 1973, *J. Am. Ceram. Soc.* 56, 518.
143. *Idem*, 1979, *ibid.* 62, 428.
144. G. Himsolt, H. Knoch, H. Huebner and F.W. Kleinlein, 1979, *ibid.* 62, 29.
145. J.B. Kessler, J.E. Ritter, Jr., and R.W. Rice, 1974, *Mater. Sci. Res.* 7, 529.
146. K.E. Puttick, 1980, *J. Phys. D.* 13, 2249.

31.

- 147. P.M. Sargent and T.F. Page, 1981, Scripta Metall., in press.
- 148. R.W. Davidge, 1967, J. Mater. Sci. 2, 339.
- 149. F. Sato and K. Sumino, 1980, ibid. 15, 1625.
- 150. J.R. Patel and A.R. Chaudhuri, 1966, Phys. Rev. 143, 601.
- 151. J.R. Patel and L.R. Testardi, 1977, Appl. Phys. Lett. 30, 3.
- 152. P.B. Hirsch, 1979, J. Physique Coll. 40, C-6, 117.
- 153. B. North and K.E. Gilchrist, 1981, J. Am. Ceram. Soc., in press.

11. GLOSSARY

| | |
|--|--|
| HPSC | hot-pressed SiC |
| PDSN | pyrolytically-deposited Si ₃ N ₄ |
| RBSN | reaction-bonded Si ₃ N ₄ |
| HPSN | hot-pressed Si ₃ N ₄ |
| KHN | Knoop hardness number (kgfmm ⁻²) |
| VHN = H | Vickers hardness number (kgfmm ⁻²) |
| n | Meyer index |
| T _m | absolute melting point (K) |
| E _g | electronic band gap (eV) |
| θ _D | Debye temperature (K) |
| E | Young's modulus (GPa) |
| ν | Poisson's ratio |
| a | indentation radius |
| b | plastic zone radius |
| c _r = c | radial crack radius |
| c _m | median crack radius |
| c _l | lateral crack radius |
| P | applied load |
| K _{IC} | fracture toughness (MPam ^{1/2}) |
| P* | minimum load required to cause a crack nucleus to form. |
| c* | minimum size of crack nucleus which may propagate (at P>P*). |
| β ₀ , λ ₀ , μ ₀ | constants |

12. APPENDIX 1 HARDNESS AS A FUNCTION OF LOAD

The variation of hardness with applied load (the load sensitivity or indentation size effect (15)) is quantified by the Meyer index (n) defined by (16):

$$P = ka^n \quad k = \text{constant}$$

A value of $n = 2$ indicates no variation of hardness with load:
 $H \propto P/a^2 = \text{constant}$ with respect to load.

For $n < 2$, the hardness decreases with increasing load; for $n > 2$, the converse is true.

The variation of n with temperature for all the materials investigated is summarised in Table A1, n being calculated from a least-squares fit to a $\ln a : \ln P$ plot by measuring the errors in $\ln a$ (15). Most of the indices are in the range 1.9-2, indicating relatively little load sensitivity over the load range used (100 gf - 1 kgf). PDSN and reaction-bonded SiC have relatively low values of n (~ 1.8 at room temperature), whilst RBSN and NC132 hot-pressed Si_3N_4 have Meyer indices greater than 2 at high temperatures - generally n tends to increase slightly with increasing temperature for all materials.

Somewhat lower values of Meyer index have been reported for a few of these materials: for example, workers in Cambridge (10, 11, 15, 16) have found ~ 1.65 for NC203 hot-pressed SiC and ~ 1.7 for NC132 hot-pressed Si_3N_4 ; Chakraborty and Mukerji (136) have reported $\sim 1-1.5$ for various reaction-bonded and single crystal silicon nitrides. All these studies were made at lower loads than used here (e.g. up to 100 gf (16); 100-500 gf (136)), the load sensitivity being more pronounced at lower loads.

Possible origins of the indentation size effect have been discussed (15, 16) but are difficult to determine for any particular material. Specimen microstructure is thought to play a particularly significant role in impeding motion of the extending plastic yield front at increasing loads, and a pronounced indentation size effect is expected where the microstructure is on the same scale as the sub-indentation plastic zone (15, 16). This is the case for PDSN (grain size $\sim 50\mu\text{m}$), all the other materials having grain sizes much smaller than the indentation size (except, of course, the single crystals). This may account for the relatively low value of n for PDSN.

As mentioned previously, it was found impossible to measure high-load (> 200 gf), low-temperature ($< 300^\circ\text{C}$) indentation diagonals in {111} single crystal Si: due to excessive cracking (fig. 9). However, Meyer indices based on 100 and 200 gf indentations have been calculated: at room temperature, ~ 1.1 and at 200°C , ~ 1.3 . No explanation for these low values is yet offered, but they may account for the relatively low value of n for reaction-bonded SiC, which contained ~ 12 vol.% unreacted Si in the microstructure.

The high n values for RBSN and NC132 at 800°C are interesting, but again no explanation is offered.

Porosity effects have been discussed by Chakraborty and Mukerji (136): for reaction-bonded silicon nitrides, n was found to decrease with increasing porosity. No such effect has been found in this investigation - the porous materials (sintered silicon carbides and RBSN) have Meyer indices similar to those of the fully dense materials.

Finally, it is instructive to consider how further investigations might shed light on this relatively poorly-understood subject. Of prime importance is an understanding of elastic recovery effects in these stiff materials (147): on unloading the indenter, the specimen relaxes elastically hence the indentation size (and therefore hardness) under load is different from the final measured size. The load sensitivity of this effect must be quantified before other effects (e.g. indentation fracture, strain rate, surface effects, dislocation effects) may be evaluated. The origins of load sensitivity in a particular material may well remain obscure until details of all the deformation mechanisms acting during indentation are known. To this end, TEM and other high resolution investigations of indentation plasticity mechanisms are crucial (see section 2.2).

13. APPENDIX 2 HARDNESS AS A FUNCTION OF IMPURITY CONTENT

Impurity effects on dislocation mobility have been reported for many brittle materials, especially ionic solids (e.g. 31, 32, 37, 85, 148, 149). In MgO, for instance, Fe^{3+} impurities produce solid solution hardening effects (148), dislocation velocities being limited by the Peierls stress below a concentration of ~ 200 p.p.m. Fe^{3+} at high resolved shear stresses (37). Trivalent impurities in MgO impede screw dislocations athermally, whilst divalent cations are thought to retard edge dislocations at high temperatures by the formation of Cottrell atmospheres (149). Dislocation pinning is often by impurity-vacancy dipoles in alkali halides (e.g. 31), in which such hardening effects are more pronounced (148). At high impurity concentrations, precipitation hardening produces even larger effects (e.g. 85, 148).

Covalent semiconductors such as Si and Ge also show variations of dislocation velocity with dopant (150, 151) which have been modelled by Hirsch (152). The formation of double kinks on partial dislocations is considered to generate acceptor/donor levels in the band gap, and electron/hole transitions may occur to these levels, resulting in changes in the concentration of charged kinks (hence dislocation velocity, since this is proportional to total kink concentration). The factors determining this change are complex since the kink energy levels are a function of both the material and the structure of the dislocations produced. Temperature and dopant concentration (donor or acceptor) are also variables in this process. Thus, screw dislocations in Si at 600°C are more mobile in doped (n or p) materials, above a critical impurity concentration. In Ge at 800°C , 60° dislocations are more mobile in n-type than in p-type material (again, above a certain critical impurity level) and undoped Ge shows an intermediate 60° dislocation mobility.

An experimental study of the hot-hardness behaviour of transistor grade n and p-type {111} single crystal Si* was undertaken, the results being summarised in table A2.1. The hardness/temperature curves proved identical to within experimental errors and possible explanations are given below. A series of REFEL reaction-bonded silicon carbides of varying impurity content and major polytype were indented at room temperature under ambient conditions using a Leitz 'Miniload' microhardness tester (1 kgf Vickers indentations), and the results are presented in table A2.2. Precise impurity levels were not known, but were of the order of 1000 p.p.m. for each major dopant, the Al-doped specimen also containing ~ 500 p.p.m. of nitrogen, and the 'undoped' sample ~ 300 p.p.m. of various impurities (notably Fe, Al, N) (153). Alpha materials showed no variation of hardness with dopant, whilst undoped β -REFEL appeared harder than B-doped (p-type) material. However, this latter effect might have been due to other microstructural factors, such as a comparative lack of residual Si in the undoped specimen. In any case, the major polytype present in the material appears to be more important in determining hardness than the impurity concentration.

A number of points arise out of this investigation. Firstly, the

* The nature and concentration of the dopants in these samples were unfortunately not known, but resistivity values are quoted in table A2.1.

extent to which hardness reflects dislocation mobility is open to question in these materials, especially at low homologous temperatures (see section 2.3), so the negative results presented here must be treated with caution. In the case of the silicon slices, dopant levels might conceivably have been below those required to significantly affect dislocation mobility (152), and in any event the effect may occur equally in both n and p-type materials, as reported for high-temperature screw dislocations in Si (e.g. 152). In attempting to predict hardening/softening effects, the nature of dislocation structures resulting from indentation must be well characterized - the contributions of dopant effects to the mobility of each type of dislocation may then be summed in order to evaluate the overall effect. In general this is impossible due to lack of experimentally-obtained information on dislocation structures beneath indentations (as a function of temperature) on the one hand and lack of theoretical knowledge of the energy levels resulting from kinks in various types of partial dislocation on the other.

The effect of dopant concentration on hardness is therefore best investigated empirically and, to this end, further, more detailed experiments will obviously be required. Thus, a range of well-characterized pure, lightly doped and heavily doped n and p-type materials should be used, and sub-indentation dislocation structures investigated (e.g. by TEM) as thoroughly as possible.

14. APPENDIX 3 HARDNESS AS A FUNCTION OF SURFACE FINISH

Table A3 summarizes the results of an experiment to determine the effect of surface finish on the room temperature Vickers hardness of alpha REFEL reaction-bonded SiC. The same specimen was used throughout the experiment, using a Kent polishing machine equipped with automatic polishing arm and utilizing constant wheel speed and applied weight (1.75 kg). The sequence described represents typical polishing procedure for this and similar materials, starting with coarse diamond compound on metal laps and finishing with fine (in this case 1/10 μ m) diamond compound on a soft cloth polishing wheel. Additionally, the material was polished for a longer period of time (2 hrs. in total) at the 1/10 μ m stage, in case the normally used time of 15 min. proved insufficient to remove damage from the coarser polishing stages. The surface was then roughened to 6 μ m and then 14 μ m (cloth) finishes as a consistency check.

At each stage in the polishing procedure, the amount of damage in the specimen surface was assessed by optical microscopy (attempts to quantify this by measuring cathodoluminescent output in a SEM failed, since the material showed no output whatever), and the specimen was indented at 100 gf and 1 kgf loads (10 indentations each). For this, a Leitz 'Miniload' microhardness tester with Vickers indenter was used, tests being made at room temperature under ambient conditions. Since the measured effect was likely to depend on the sampling depth of the indenter, penetration depths were calculated ($d/h\sqrt{7}$ for Vickers indentations, where d = diagonal length and h = penetration depth), being typically 1 μ m for 100 gf indentations and 4 μ m for 1 kgf indentations.

It was found impossible to resolve indentations on the coarsely-finished surfaces (14 μ m and 6 μ m cast iron laps) due to surface roughness, the material being severely chipped and scratched. After the 6 μ m copper lap, the sample showed small unchipped regions and, macroscopically, a slight lustre. When polished on the 6 μ m cloth, the specimen appeared shiny, optical examination revealing only tiny (\sim 1 μ m) chips in the surface, especially around the SiC: Si interfaces present in this material (1). After the 1 μ m and subsequent stages, no damage could be resolved by optical microscopy, until roughened to 6 μ m and finally 14 μ m cloth finish, where the damage was again marked, although not as severe as with the 6 μ m copper lap.

The results show that at 1 kgf applied load, the macroscopically shiny surfaces (6 μ m - 1/10 μ m cloths) all showed similar hardness values (\sim 2050 kgfmm⁻²) to well within experimental errors. Only the highly damaged 6 μ m copper-lapped and 14 μ m cloth-lapped surfaces showed a hardening effect, in proportion to the amount of damage observed.

The 100 gf indentations provided a slightly more sensitive test, revealing hardening effects at the 6 μ m cloth stages with respect to the highly-polished 1-1/10 μ m finishes. In neither case did the hardness change significantly on polishing for a long period of time at the 1/10 μ m stage. (N.B. errors quoted in table A3 are 95% confidence limits.)

In conclusion, a hardening effect has been observed on the surface of an alpha REFEL reaction-bonded SiC when subjected to optically resolvable amounts of abrasion damage. The effect was most pronounced for small indentation sampling depths, i.e. at low applied loads, and

was only observed when the scale of the abrasion damage was of the order of, or greater than, the depth of indentation. The mechanism(s) responsible for this effect have not been determined - detailed TEM observations of the deformation structures involved in both indentation and abrasion processes will be required to do this.

| MATERIAL | SOURCE | Main Polytype | Grain Size # |
|--------------------------|---|--|--|
| <u>SILICON CARBIDE</u> | | | |
| (0001) single crystal | Arendal Smelteverk (Norway) | α (13) | - |
| Hot-pressed | Norton NC203 | α (10) | $\sim 5\mu\text{m}$ |
| Sintered (a) | Carborundum Co. | α (*) | $\sim 10\mu\text{m}$ |
| (b) | Experimental batch from Prof.H.Suzuki (130) | α (130) | Needles: Length $\sim 20\mu\text{m}$ Width $\sim 2\mu\text{m}$ |
| Reaction-bonded | UKAEA, Springfield | α (12) | a) $\sim 10\mu\text{m}$ b) $\sim 5\mu\text{m}$ |
| <u>SILICON NITRIDE</u> | | | |
| Pyrolytically-deposited | Admiralty Marine Technology Estab., Holton Heath. | α (131) | $\sim 50\mu\text{m}$ |
| Reaction-bonded | Ford '2.7' | 80wt% α 20wt% β (132) | $\sim 1\mu\text{m}$ |
| Hot-pressed (a) | Norton NC132 | largely β (132) | $\lesssim 5\mu\text{m}$ |
| (b) | Norton NCX34 | largely β (132) | $\sim 5\mu\text{m}$ some grains $\sim 20\mu\text{m}$ |
| <u>SILICON</u> | | | |
| {111} single crystal (n) | Texas Instruments (U.K.) | - | - |
| {111} single crystal (p) | | | |

*Carborundum Technical Data Sheet

+UKAEA Technical Data Sheet

Measured from optical/SEM images

Table 1. Properties of the materials investigated. Vickers hardnesses values were obtained in this investigation and have been averaged over the load range used and finally expressed as a projected area Vickers hardness value.

| Porosity # | ROOM TEMPERATURE VALUES | | | |
|--|------------------------------|--|--|---|
| | Young's Modulus (E) (GPa) | Vickers Hardness (H) (GPa) | Fracture Toughness (K _{IC}) (MPa \sqrt{m}) | Poisson's Ratio (ν) |
| - | 446 (109) | 35.6 [± 0.6] | 3.4 (133) | 0.2 (135) |
| - | 438 (25) | 31.7 [± 0.7] | 6.1 (133) | 0.17 (132) |
| 4.5 vol. % | 406 (*) | 29.9 [± 0.4] | 4.6 (*) | 0.15 (*) |
| 9 vol. % | 400 (estimated) | 25.7 [± 0.3] | - | - |
| None, but 12-14 vol. % unreacted silicon | 400 (+) | 25.4 [± 1] | 4.4 (133) | 0.24 (+) |
| small amount (not measured) | 312 (131) | 37.0 [± 1] | - | - |
| 13 vol. % (132) | 210 (132) | 15.3 [± 0.3] | - | 0.22 (132) |
| - | 320 (132) | 21.7 [± 0.3] | 5.0 (132) | 0.27 (132) |
| - | 310 (132) | 18.1 [± 0.2] | 5.9 (132) | 0.27 (132) |
| - | 168 (124) | 18.7 [± 0.3] 19.2 [± 0.2] | 0.8 (134) | 0.27 (23) (polycrystalline value) |

Table 1 (cont.)

| <u>MATERIAL</u> | <u>INDENTER</u> | <u>TEMP. RANGE</u> <u>INVESTIGATED</u> |
|---------------------------------|-------------------|---|
| <u>SILICON CARBIDE</u> | | |
| (0001) single crystal | Knoop Vickers* | Room Temp. - 800°C Room Temp. & 800°C (only) |
| Hot-pressed (Norton NC203) | Knoop Vickers* | Room Temp. - 800°C " |
| Sintered (a) (Carborundum) | Knoop | " |
| | Vickers* | " |
| (b) (Suzuki) | Vickers* | " |
| Reaction-bonded (a) | Knoop | Room Temp. - 900°C |
| (REFEL - two grades) (b) | Vickers | Room Temp. - 800°C |
| <u>SILICON NITRIDE</u> | | |
| Pyrolytically-deposited | Vickers* | Room Temp. - 800°C |
| Reaction-bonded (Ford '2.7') | Vickers* | " |
| Hot-pressed (a) (Norton NC132) | Vickers* | " |
| (b) (Norton NCX34) | Vickers* | " |
| <u>SILICON</u> | | |
| {111} single crystal (n-type) | Vickers* | Room Temp. - 800°C |
| {111} single crystal (p-type) | Vickers | |

Table 2. A summary of experimental work performed to date. * indicates crack lengths were measured for indentation fracture mechanics analysis.

| TEMP. (°C) | (0001) SiC | HPSC (NC203) | Sintered SiC | | RBSC (REFEL) | PDSN | RBSN (Ford 2.7) | HPSN | | {111} Si (n) |
|---------------|---------------|-----------------|---------------|----------|-----------------|------|--------------------|---------|---------|-----------------|
| | | | (Carborundum) | (Suzuki) | | | | (NC132) | (NCX34) | |
| 24 | 2.33 | 2.45 | 2.43 | 2.60 | 2.66 | 1.91 | 2.44 | 2.53 | 2.73 | |
| 100 | | 2.66 | | | 2.76 | 1.97 | | 2.65 | | |
| 200 | | 2.68 | 2.56 | 2.85 | 2.94 | 1.98 | 2.48 | 2.74 | 2.85 | |
| 300 | | | | | 3.13 | 1.98 | | | | 2.8 |
| 400 | | 3.08 | 2.85 | 3.25 | 3.36 | 2.12 | 2.58 | 2.70 | 3.04 | 3.1 |
| 500 | | | | | | | | | | 3.5 |
| 600 | | 3.43 | 3.29 | 3.74 | 4.0 | 2.22 | 2.5 | 2.90 | 3.23 | 4.5 |
| 700 | | | | | | | | | | 6.3 |
| 800 | 3.47 | 3.93 | 3.73 | 4.00 | 4.66 | 2.42 | 2.63 | 3.06 | 3.4 | 8.4 |

Table 3. The ratio (b/a) of plastic zone radius to Vickers indentation radius at constant applied load (1kgf) as a function of temperature for SiC & Si₃N₄ materials and {111} single crystal Si. Standard errors typically ± 0.07 .

| TEMP. (°C) | (0001) SiC | HPSC (NC203) | Sintered SiC | | PDSN | (Ford 2.7) | HPSN | | {111} Si (n) |
|---------------|---------------|-----------------|---------------|----------|------|------------|---------|---------|-----------------|
| | | | (Carborundum) | (Suzuki) | | | (NC132) | (NCX34) | |
| 24 | 3.7 | 2.3 | 3.4 | 2.0 | 3.3 | 1.8 | 1.7 | 1.8 | |
| 100 | | 2.2 | | | 3.5 | | 1.7 | | |
| 200 | | 2.6 | 3.6 | 2.7 | 3.6 | 1.9 | 1.7 | 1.9 | |
| 300 | | | | | 3.7 | | | | 3.4 |
| 400 | | 2.5 | 3.5 | 2.6 | 3.6 | 1.9 | 1.6 | 1.8 | 3.9 |
| 500 | | | | | | | | | 4.1 |
| 600 | | 2.3 | 3.4 | 2.4 | 4.3 | 2.0 | 1.5 | 1.9 | 3.3 |
| 700 | | | | | | | | | 2.7 |
| 800 | 4.3 | 2.0 | 3.2 | 2.1 | 3.6 | 1.9 | 1.5 | 2.0 | 0 |

Table 4. The ratio (c/a) of radial crack radius to Vickers indentation radius at constant applied load (1kgf) as a function of temperature for SiC & Si_3N_4 materials and {111} single crystal Si. Standard errors typically ± 0.1

| TEMP. (°C) | (0001) SiC | HPSC (NC203) | Sintered SiC | | PDSN | RBSN (Ford 2.7) | HPSN | | {111} Si (n) |
|---------------|---------------|-----------------|---------------|----------|------|--------------------|---------|---------|-----------------|
| | | | (Carborundum) | (Suzuki) | | | (NC132) | (NCX34) | |
| 24 | 1.6 | 0.9 | 1.4 | 0.8 | 1.7 | 0.7 | 0.7 | 0.7 | |
| 100 | | 0.8 | | | 1.8 | | 0.6 | | |
| 200 | | 1.0 | 1.4 | 1.0 | 1.8 | 0.8 | 0.6 | 0.7 | |
| 300 | | | | | 1.9 | | | | 1.2 |
| 400 | | 0.8 | 1.2 | 0.8 | 1.7 | 0.7 | 0.6 | 0.6 | 1.2 |
| 500 | | | | | | | | | 1.2 |
| 600 | | 0.7 | 1.0 | 0.6 | 1.9 | 0.8 | 0.5 | 0.6 | 0.7 |
| 700 | | | | | | | | | 0.4 |
| 800 | 1.3 | 0.5 | 0.9 | 0.5 | 1.5 | 0.7 | 0.5 | 0.6 | 0 |

Table 5. The ratio (c/b) of radial crack radius to plastic zone radius at constant applied load (1kgf) as a function of temperature for SiC and Si_3N_4 materials and {111} single crystal Si. Standard errors typically ± 0.1 .

| TEMP. (°C). | (0001) SiC | HPSC (NC203) | Sintered SiC | | PDSN | RBSN (Ford 2.7) | HPSN | | {111} Si (n) |
|----------------|---------------|-----------------|---------------|----------|------|--------------------|---------|---------|-----------------|
| | | | (Carborundum) | (Suzuki) | | | (NC132) | (NCX34) | |
| 24 | 1.7 | 3.4 | 1.8 | 3.6 | 1.7 | 2.8 | 4.2 | 3.5 | 0.5 |
| 100 | | 3.3 | | | 1.5 | | 4.1 | | 0.7 |
| 200 | | 2.5 | 1.7 | 2.1 | 1.5 | 2.4 | 3.9 | 3.2 | 0.6 |
| 300 | | | | | 1.4 | | | | 0.8 |
| 400 | | 2.6 | 1.5 | 2.2 | 1.3 | 2.5 | 4.2 | 3.2 | 0.6 |
| 500 | | | | | | | | | 0.6 |
| 600 | | 2.7 | 1.5 | 2.2 | 1.0 | 2.3 | 4.2 | 2.7 | 0.6 |
| 700 | | | | | | | | | 0.8 |
| 800 | 1.0 | 3.0 | 1.5 | 2.5 | 1.2 | 2.4 | 4.3 | 2.6 | - |

Table 6. Indentation fracture toughness values for SiC and Si_3N_4 materials and {111} single crystal Si as a function of temperature. Standard errors typically ± 0.3 .

| TEMP. (°C) | (0001) SiC | HPSC (NC203) | Sintered SiC | | RBSC (REFEL) | PDSN | RBSN (Ford 2.7) | HPSC | | {111} Si (n) |
|---------------|---------------|-----------------|---------------|----------|-----------------|------|--------------------|---------|---------|-----------------|
| | | | (Carborundum) | (Suzuki) | | | | (NC132) | (NCX34) | |
| 24 | 1.93 | 1.88 | 1.87 | 1.93 | 1.80 | 1.78 | 1.94 | 1.97 | 1.89 | - |
| 200 | - | 1.96 | 1.92 | 1.92 | 1.87 | 1.77 | 2.07 | 1.98 | 2.00 | - |
| 400 | - | 1.88 | 1.96 | 1.97 | 1.89 | 1.85 | 2.02 | 2.11 | 1.94 | 1.86 |
| 600 | - | 1.86 | 2.02 | 1.99 | 1.99 | 1.89 | 2.09 | 2.01 | 1.95 | 1.95 |
| 800 | 1.92 | 1.99 | 1.88 | 1.97 | 1.91 | 2.05 | 2.11 | 2.23 | 2.04 | 1.95 |

Table A1. Variation of Meyer index (n) with temperature for Vickers indentations in the load range 100gf - 1kgf. Standard errors typically ± 0.03 .

| TEMPERATURE (°C) | Vickers Hardness (kgfmm^{-2}): {111} Si | |
|---------------------|--|--|
| | p-type ($\rho = 7.05 \text{ } \Omega\text{cm}$) | n-type ($\rho = 9.15 \text{ } \Omega\text{cm}$) |
| 24 | 1814 (± 21) | 1790 (± 36) |
| 200 | 1212 (± 29) | 1308 (± 27) |
| 400 | 804 (± 12) | 795 (± 8) |
| 500 | 464 (± 5) | 457 (± 5) |
| 600 | 329 (± 10) | 336 (± 9) |
| 800 | 92 (± 1) | 96 (± 1) |

Table A2.1. The effect of dopant on the Vickers hardness of {111} single crystal Si as a function of temperature. Applied load = 100gf in each case. Errors are one standard error in the mean for 10 indentations.

| Material | Vickers hardness (kgfmm^{-2}) |
|--------------------------|--|
| Undoped α REFEL | 2070 (± 60) |
| Al-doped α REFEL | 2060 (± 40) |
| AlN-doped α REFEL | 2060 (± 60) |
| B-doped α REFEL | 2145 (± 110) |
| Undoped β REFEL | 2560 (± 30) |
| B-doped β REFEL | 2350 (± 70) |

Table A2.2. The effect of dopant on the room temperature Vickers hardness of α and β REFEL reaction-bonded silicon carbides. Applied load = 1kgf in each case. Errors are 95% confidence limits (10 indentations).

| Polishing Sequence | Time (min.) | Vickers Hardness (kgfmm ⁻²) | |
|--|-------------|---|-------------|
| | | (100gf load) | (1kgf load) |
| 14μm diamond compound on cast iron lap | 5 | - | - |
| 6μm " " " " | 10 | - | - |
| 6μm " " " copper lap | 15 | - | 2690 (±250) |
| 6μm " " " Hyprocel Pellon cloth | 45 | 2930 (±190) | 2070 (±100) |
| 1μm " " " micro cloth | 15 | 2440 (±110) | 2010 (±100) |
| $\frac{1}{4}\mu\text{m}$ " " " " | 15 | 2570 (±150) | 2090 (±50) |
| $\frac{1}{10}\mu\text{m}$ " " " " | 15 | 2470 (±200) | 2060 (±85) |
| $\frac{1}{10}\mu\text{m}$ " " " " | 120 | 2560 (±160) | 2040 (±50) |
| *6μm " " " Hyprocel Pellon cloth | 15 | 2710 (±190) | - |
| *14μm " " " " | 15 | 2970 (±310) | 2430 (±190) |

Table A3. The effect of surface finish on the room temperature Vickers hardness of alpha REEEL reaction-bonded silicon carbide. Indentation penetration depths were ~1μm for 100gf and ~4μm for 1 kgf load. *Indicates the surface was roughened from 1/10μm finish. Errors are 95% confidence limits (10 indentations).

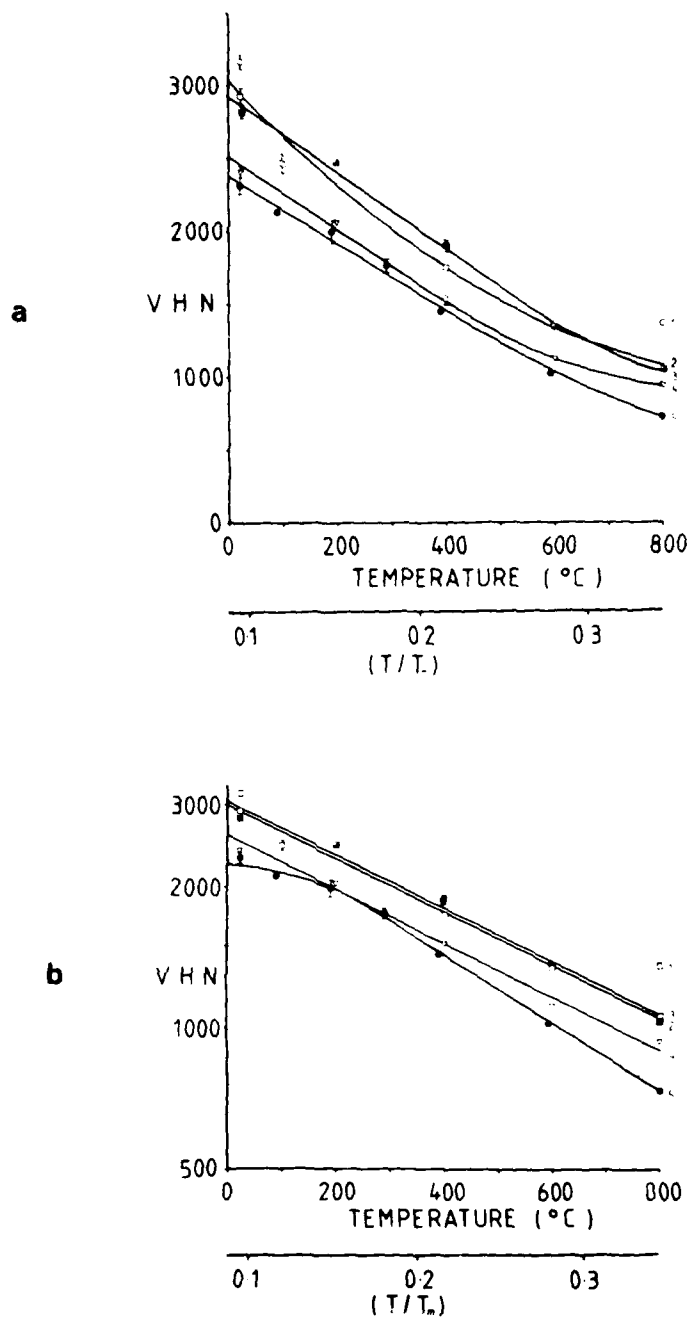


Figure 1. The variation of Vickers hardness (1 kgf applied load) with temperature for SiC materials: (a) linear, (b) logarithmic hardness scales. Curve 1 = (0001) single crystal (open circles), curve 2 = NC203 hot-pressed (open squares), curve 3 = Carborundum sintered (filled squares), curve 4 = Suzuki sintered (open triangles), curve 5 = REFEL reaction-bonded (filled circles). Error bars indicate one standard error in the mean.

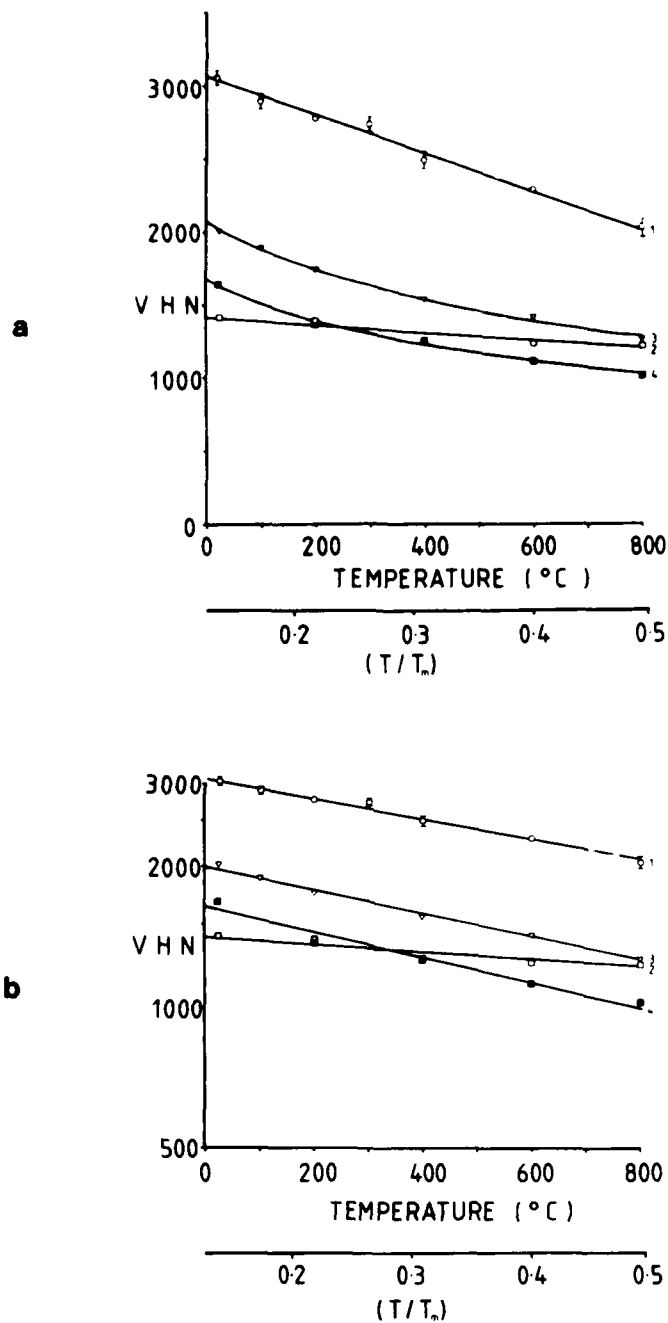


Figure 2. The variation of Vickers hardness (1 kgf applied load) with temperature for Si_3N_4 materials: (a) linear, (b) logarithmic hardness scales. Curve 1 = PDSN (open circles), curve 2 = Ford '2.7' RBSN (open squares), curve 3 = NC132 hot-pressed (open triangles), curve 4 = NCX34 hot-pressed (filled squares). Error bars indicate one standard error in the mean.

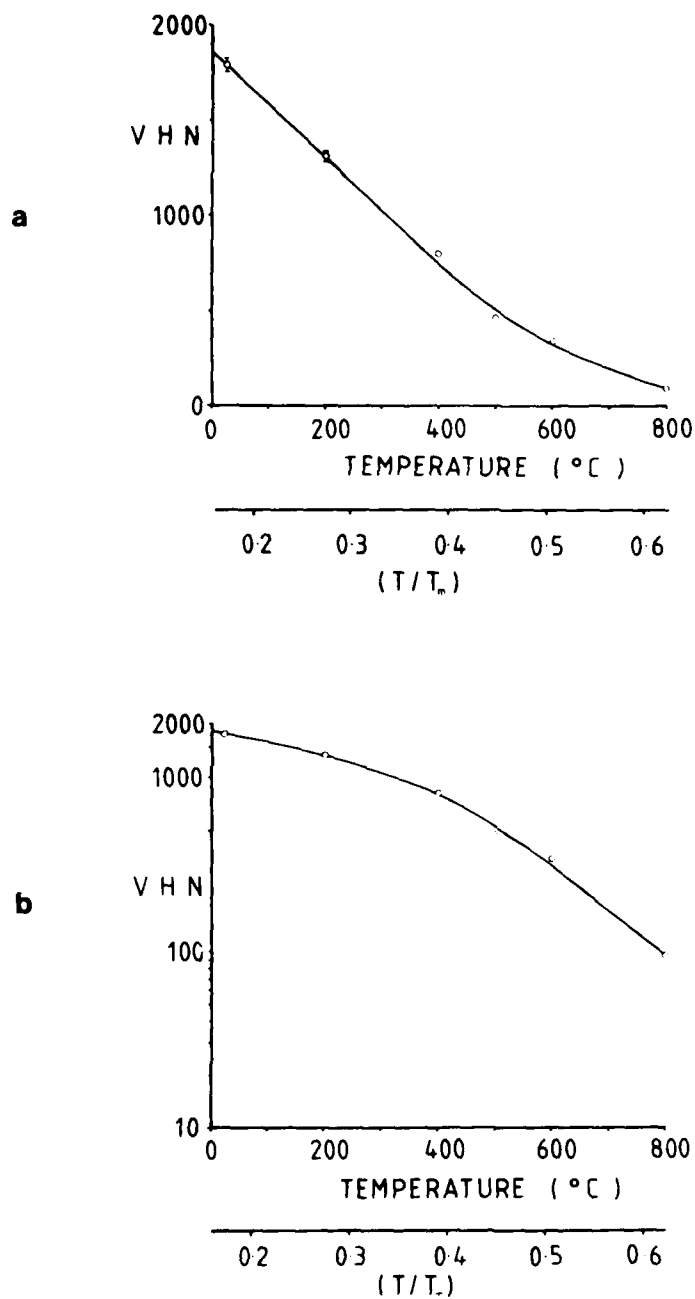


Figure 3. The variation of Vickers hardness (100 gf applied load) with temperature for n-type {111} single crystal silicon: (a) linear, (b) logarithmic hardness scales. Error bars indicate one standard error in the mean.



a

1 μm —



b

1 μm —



c

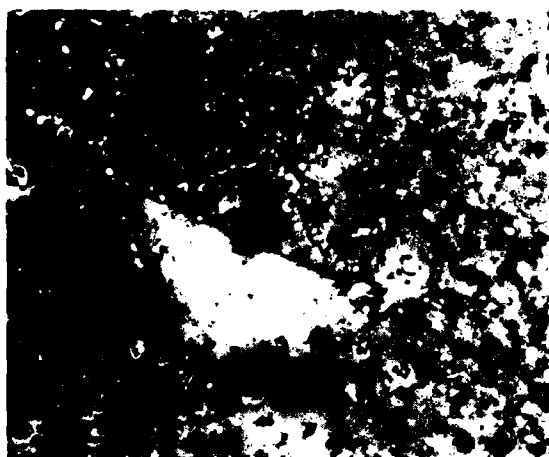
10 μm —



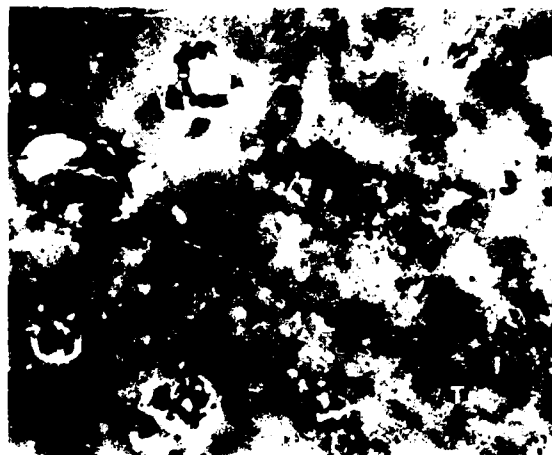
d

10 μm —

Figure 4. Fracture in a 1000 Å grain indented in a 1 kgf load in SiC: (a) room temperature indentation (1 kgf load) showing radial fracture, partly along grain boundaries (arrow); (SEM-secondary-20KV); (b) as (a) showing profile cracks and lateral cracking along a grain boundary; (c) 800°C indentation (1 kgf load) showing large-scale radial and lateral cracking which is clearly associated with grain growth in the superstructure, cracks occasionally terminating at grain boundaries (SEM-secondary-20KV); (d) as (a) showing only cracks perpendicular to the indentation (SEM-secondary).

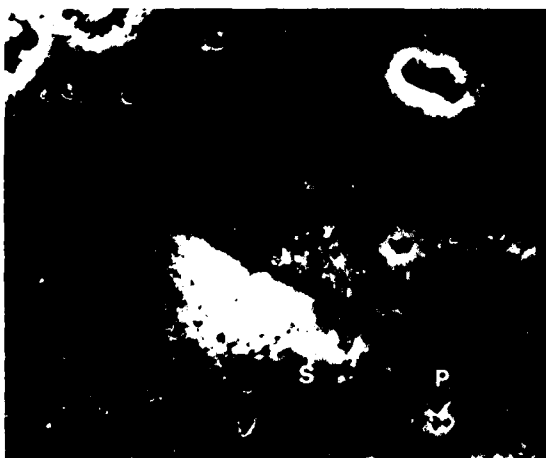


a

10 μm —————

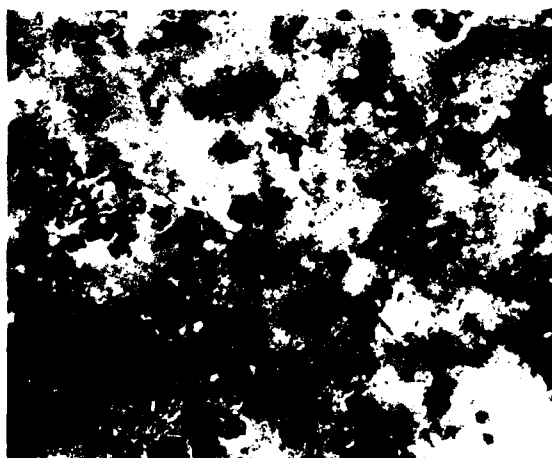
b

1 2 3 4 5 6 7 8 9 10 11 12 13 14 15 16 17 18 19 20 21 22 23 24 25 26 27 28 29 30 31 32 33 34 35 36 37 38 39 40 41 42 43 44 45 46 47 48 49 50 51 52 53 54 55 56 57 58 59 60 61 62 63 64 65 66 67 68 69 70 71 72 73 74 75 76 77 78 79 80 81 82 83 84 85 86 87 88 89 90 91 92 93 94 95 96 97 98 99 100 101 102 103 104 105 106 107 108 109 110 111 112 113 114 115 116 117 118 119 120 121 122 123 124 125 126 127 128 129 130 131 132 133 134 135 136 137 138 139 140 141 142 143 144 145 146 147 148 149 150 151 152 153 154 155 156 157 158 159 160 161 162 163 164 165 166 167 168 169 170 171 172 173 174 175 176 177 178 179 180 181 182 183 184 185 186 187 188 189 190 191 192 193 194 195 196 197 198 199 200 201 202 203 204 205 206 207 208 209 210 211 212 213 214 215 216 217 218 219 220 221 222 223 224 225 226 227 228 229 230 231 232 233 234 235 236 237 238 239 240 241 242 243 244 245 246 247 248 249 250 251 252 253 254 255 256 257 258 259 260 261 262 263 264 265 266 267 268 269 270 271 272 273 274 275 276 277 278 279 280 281 282 283 284 285 286 287 288 289 290 291 292 293 294 295 296 297 298 299 300 301 302 303 304 305 306 307 308 309 310 311 312 313 314 315 316 317 318 319 320 321 322 323 324 325 326 327 328 329 330 331 332 333 334 335 336 337 338 339 340 341 342 343 344 345 346 347 348 349 350 351 352 353 354 355 356 357 358 359 360 361 362 363 364 365 366 367 368 369 370 371 372 373 374 375 376 377 378 379 380 381 382 383 384 385 386 387 388 389 390 391 392 393 394 395 396 397 398 399 400 401 402 403 404 405 406 407 408 409 410 411 412 413 414 415 416 417 418 419 420 421 422 423 424 425 426 427 428 429 430 431 432 433 434 435 436 437 438 439 440 441 442 443 444 445 446 447 448 449 450 451 452 453 454 455 456 457 458 459 460 461 462 463 464 465 466 467 468 469 470 471 472 473 474 475 476 477 478 479 480 481 482 483 484 485 486 487 488 489 490 491 492 493 494 495 496 497 498 499 500 501 502 503 504 505 506 507 508 509 510 511 512 513 514 515 516 517 518 519 520 521 522 523 524 525 526 527 528 529 530 531 532 533 534 535 536 537 538 539 540 541 542 543 544 545 546 547 548 549 550 551 552 553 554 555 556 557 558 559 560 561 562 563 564 565 566 567 568 569 570 571 572 573 574 575 576 577 578 579 580 581 582 583 584 585 586 587 588 589 590 591 592 593 594 595 596 597 598 599 600 601 602 603 604 605 606 607 608 609 610 611 612 613 614 615 616 617 618 619 620 621 622 623 624 625 626 627 628 629 630 631 632 633 634 635 636 637 638 639 640 641 642 643 644 645 646 647 648 649 650 651 652 653 654 655 656 657 658 659 660 661 662 663 664 665 666 667 668 669 670 671 672 673 674 675 676 677 678 679 680 681 682 683 684 685 686 687 688 689 690 691 692 693 694 695 696 697 698 699 700 701 702 703 704 705 706 707 708 709 710 711 712 713 714 715 716 717 718 719 720 721 722 723 724 725 726 727 728 729 730 731 732 733 734 735 736 737 738 739 740 741 742 743 744 745 746 747 748 749 750 751 752 753 754 755 756 757 758 759 760 761 762 763 764 765 766 767 768 769 770 771 772 773 774 775 776 777 778 779 780 781 782 783 784 785 786 787 788 789 790 791 792 793 794 795 796 797 798 799 800 801 802 803 804 805 806 807 808 809 810 811 812 813 814 815 816 817 818 819 820 821 822 823 824 825 826 827 828 829 830 831 832 833 834 835 836 837 838 839 840 841 842 843 844 845 846 847 848 849 850 851 852 853 854 855 856 857 858 859 860 861 862 863 864 865 866 867 868 869 870 871 872 873 874 875 876 877 878 879 880 881 882 883 884 885 886 887 888 889 890 891 892 893 894 895 896 897 898 899 900 901 902 903 904 905 906 907 908 909 910 911 912 913 914 915 916 917 918 919 920 921 922 923 924 925 926 927 928 929 930 931 932 933 934 935 936 937 938 939 940 941 942 943 944 945 946 947 948 949 950 951 952 953 954 955 956 957 958 959 960 961 962 963 964 965 966 967 968 969 970 971 972 973 974 975 976 977 978 979 980 981 982 983 984 985 986 987 988 989 990 991 992 993 994 995 996 997 998 999 1000 1001 1002 1003 1004 1005 1006 1007 1008 1009 1010 1011 1012 1013 1014 1015 1016 1017 1018 1019 1020 1021 1022 1023 1024 1025 1026 1027 1028 1029 1030 1031 1032 1033 1034 1035 1036 1037 1038 1039 1040 1



C

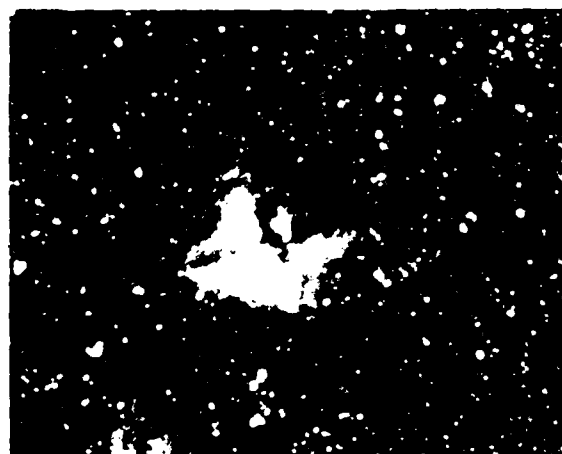
10µm —————



d

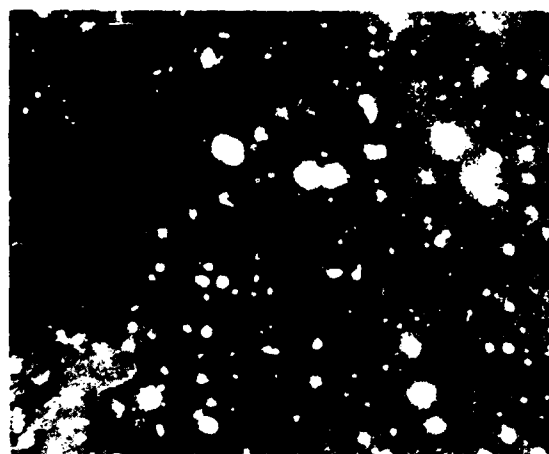
141

Figure 8. Fracture around Vickers indentations in low- T_c superconductors. The scale bar is: (a) room temperature radial fracture; (b)-(d) liquid nitrogen appears straight with small perturbations over the topographic surface of the specimen and porosity - the dense 'mottling' is probably due to secondary pores (CEM-secondary-SFV-gold coated); (e) as in (c), suggesting that radial cracks are partly intergranular (I), partly transgranular (II); (f) as (f) indentation (1 kgf load) with radial cracks I, II, III, IV, all steps (II) in a large grain adjacent to the indentation. Secondary pores form much termination sites (I) - occasional large-scale porosity may be observed (CEM-secondary-SFV-gold coated); (g) as in (c), showing partial intergrains.



a

10µm



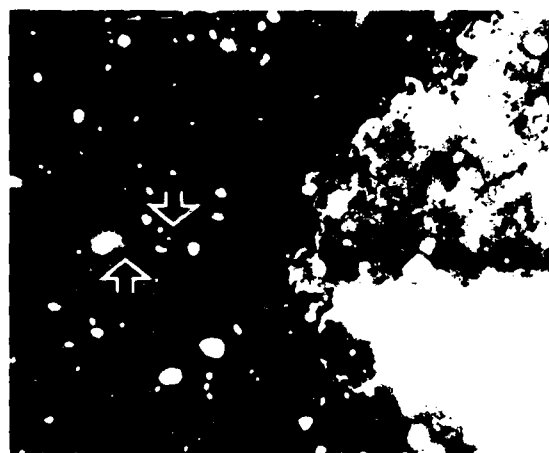
b

10µm



c

10µm



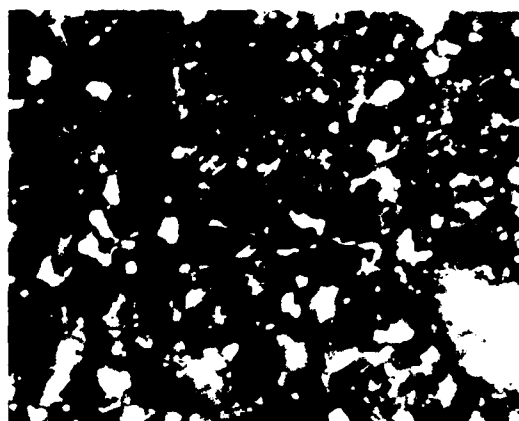
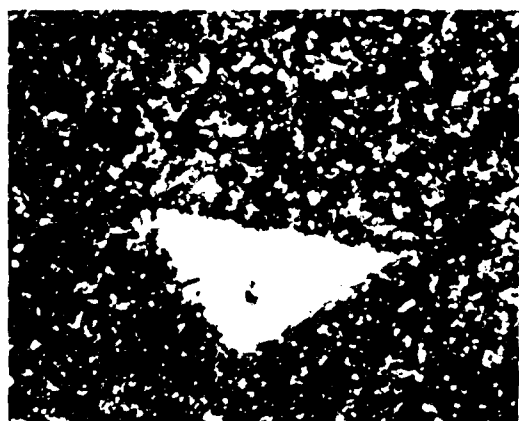
d

10µm

Figure 2. Indentation fracture in Norton 800 (composition: 60% Al₂O₃, 40% SiC): (a) room temperature indentation (1 kgf load) showing 'branching' radial cracks which are associated with the fracture of boundary WC/WC particles (white) (CEM-cement-bonded); (b) as (a) showing radial crack path at higher magnification; (c) 800°C indentation (1 kgf load) showing radial fracture surface (CEM-cement-bonded-70% gold-water); (d) as (c) showing path of crack opening (arrows) and small cracks and chips on the surface profile.



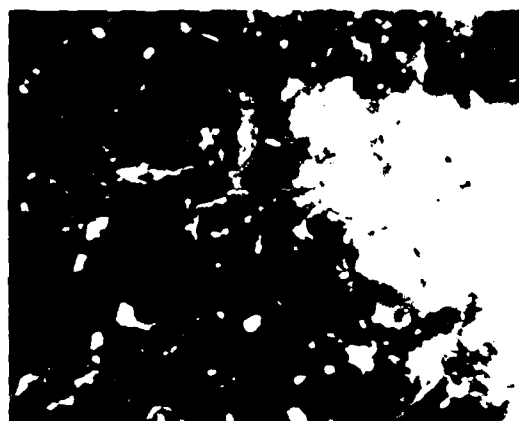
a 10 μ m

b 5443 _____

C 100 μ m



d



e



f

Figure 9. Isolation from the interval $(0, 1)$ of a sample of size $n = 100$ of the $U(0, 1)$ distribution and from the interval $(0, 1)$ of a sample of size $n = 100$ of the $U(0, 1)$ distribution with parameter $\theta = 1$ in the case of the $U(0, 1)$ distribution. The $n = 100$ showing intervals of the $U(0, 1)$ distribution and the $n = 100$ showing intervals of the $U(0, 1)$ distribution with parameter $\theta = 1$ in the case of the $U(0, 1)$ distribution.

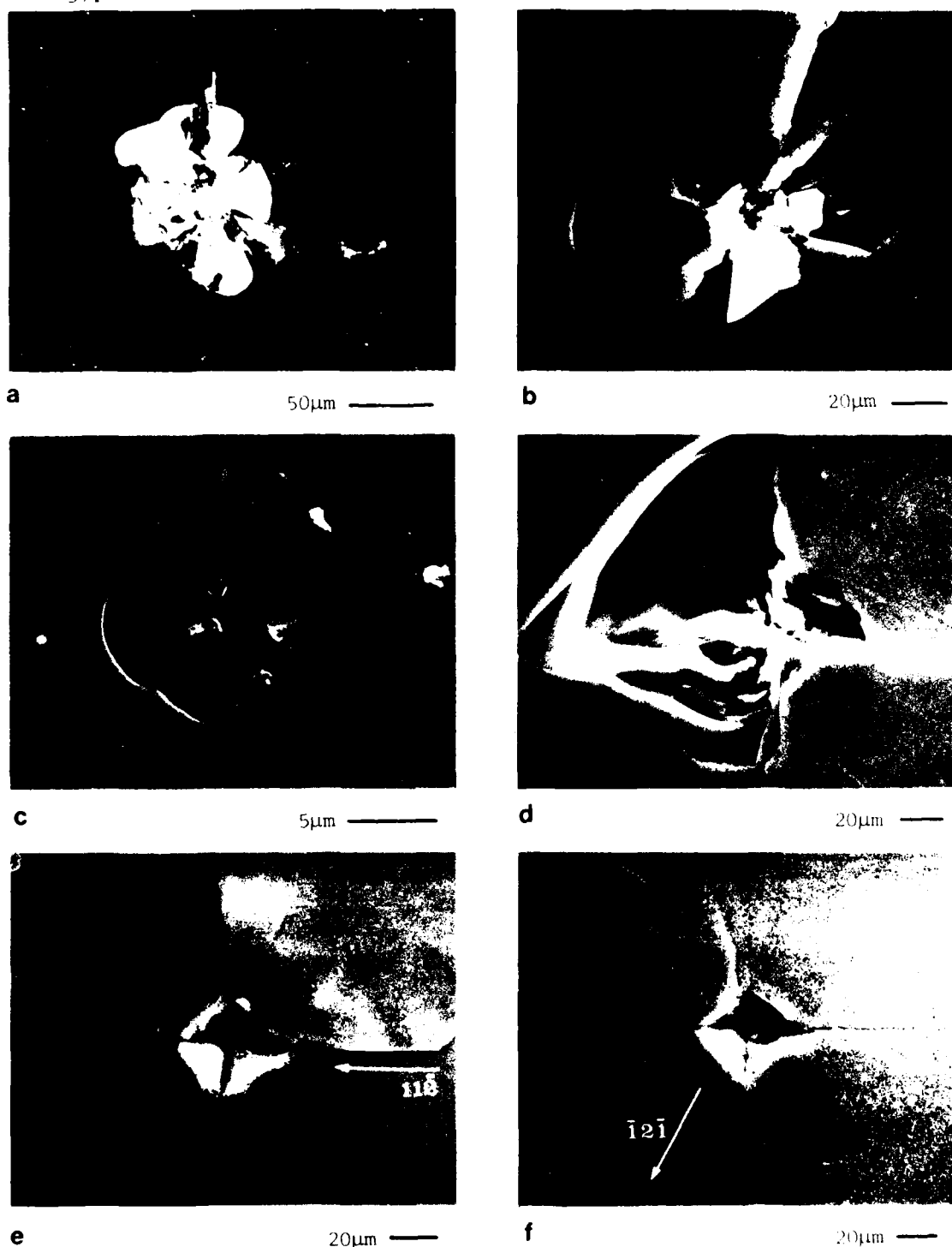
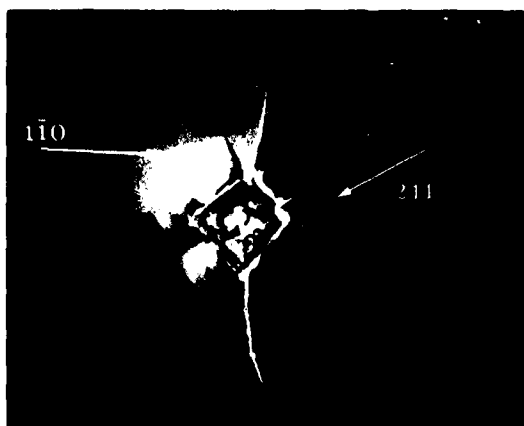
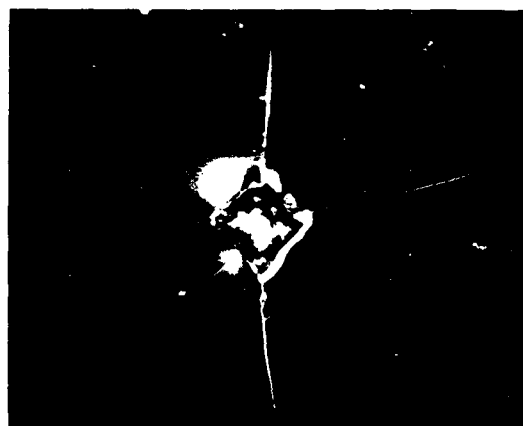


Figure 2. Vickers indentations made at various temperatures on $\{111\}$ single crystal Si (n-type) with one indenter axis parallel to $\langle 110 \rangle$. (a) Room temperature indentation with severe radial and lateral fracture (surface and subsurface). White particles may possibly be dirt (optical-Normal). (b) as (a) showing several lateral vents and subsurface cracks (SEM-secondary-30KV); (c) room temperature indentation at 100 gf load showing less extensive lateral and radial cracking (SEM-secondary-30KV); (d) 200°C indentation (1 kgf load) with massive lateral vents and radial cracks (SEM-secondary-30KV); (e) 400°C indentation (1 kgf load) showing extensive radial fracture and one subsurface lateral crack (SEM-secondary-30KV); (f) 600°C indentation (1 kgf load) showing extensive radial cracking without lateral fracture (SEM-secondary-30KV).



g

50μm



h

50μm



i

50μm



j

50μm



k

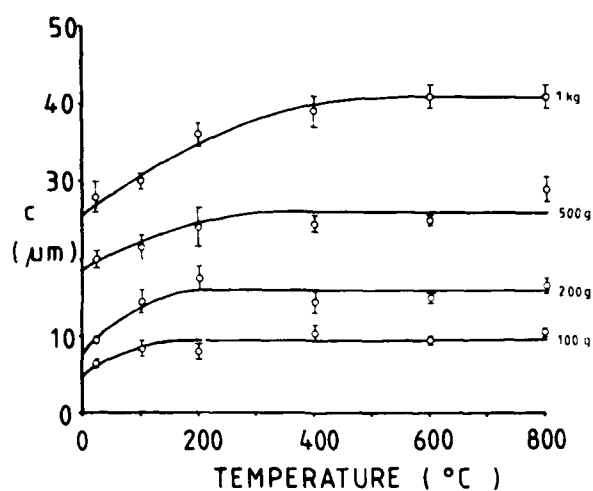
50μm



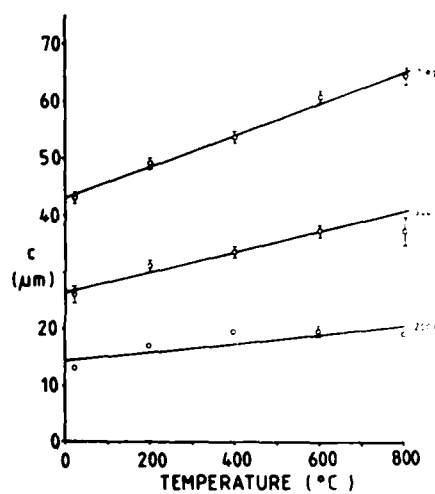
l

20μm

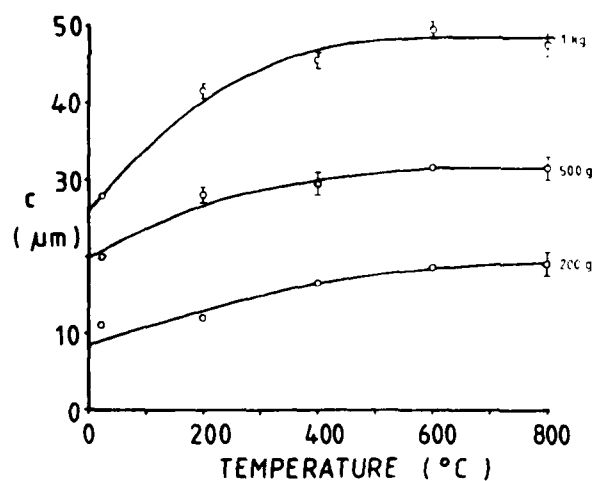
Figure 9 (cont.) (g) as (f) showing slip steps along $\langle 110 \rangle$ directions around the indentation profile (specimen was held at 500°C for ~ 20 min. after indentation). Radial cracks are mainly along $\langle 112 \rangle$ directions (optical-Nomarski); (h) as (g) with less extensive slip steps (specimen was cooled within a few minutes of indentation); (i) 600°C indentation (1 kgf load) showing more extensive slip steps and three radial cracks along $\langle 112 \rangle$ directions (optical-Nomarski); (j) 700°C indentation (1 kgf load) with highly developed slip steps and only two radial cracks, both along $\langle 110 \rangle$ directions (optical-Nomarski); (k) 800°C indentation (1 kgf load) showing no radial fracture (optical-Nomarski). (l) as (k) showing a small subsurface lateral crack and fracture within the indentation profiles (SEM-secondary-30kV).



a



b



c

Figure 10. Radial crack radius c as a function of temperature and load for SiC materials: (a) NC203 hot-pressed, (b) Carborundum sintered, (c) Suzuki sintered. Error bars indicate one standard error in the mean.

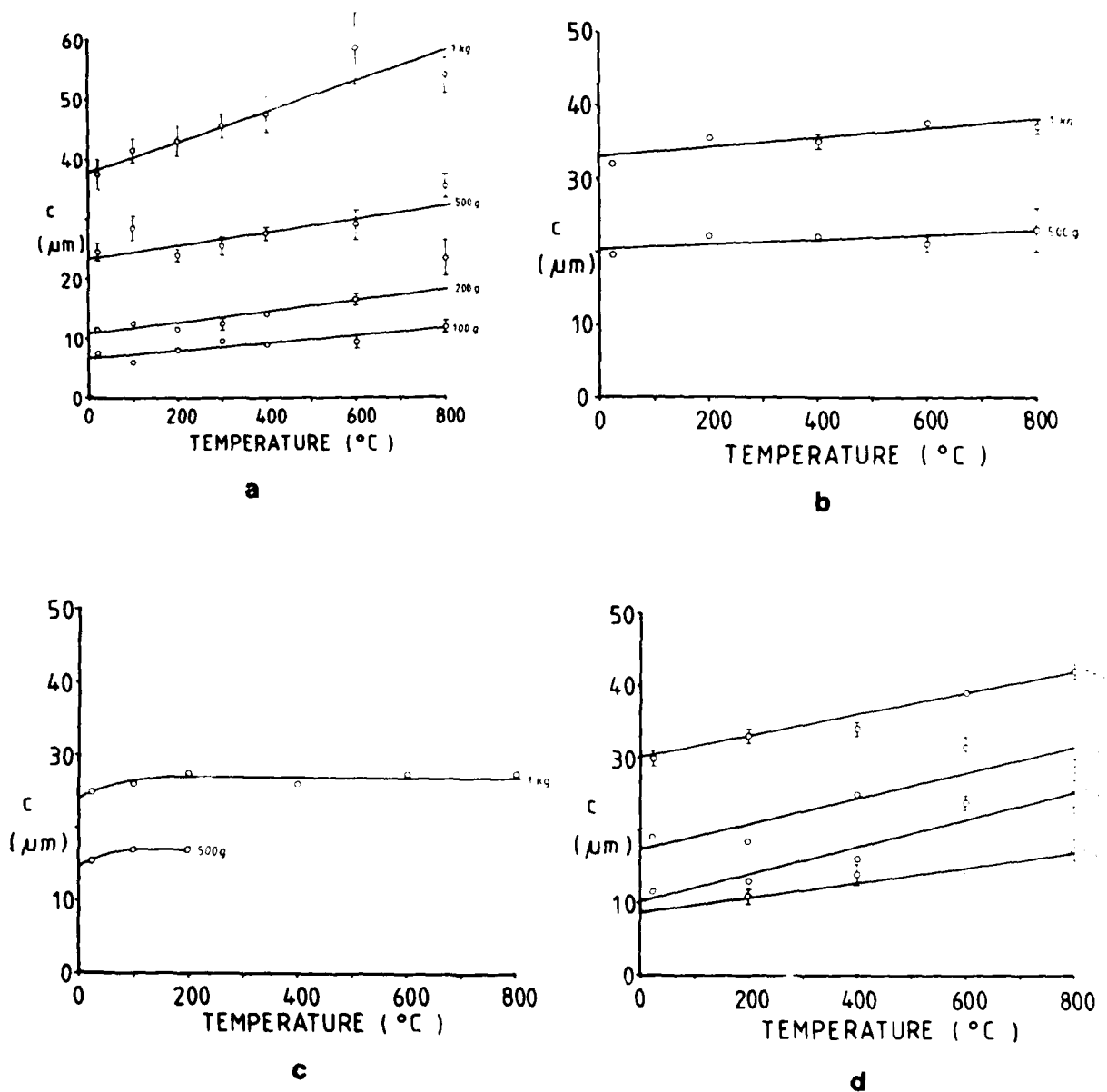


Figure 11. Radial crack radius c as a function of temperature and load for Si_3N_4 materials: (a) PDSN, (b) Ford '2.7' RBSN, (c) NC132 hot-pressed, (d) NCX34 hot-pressed. Error bars indicate one standard error in the mean.

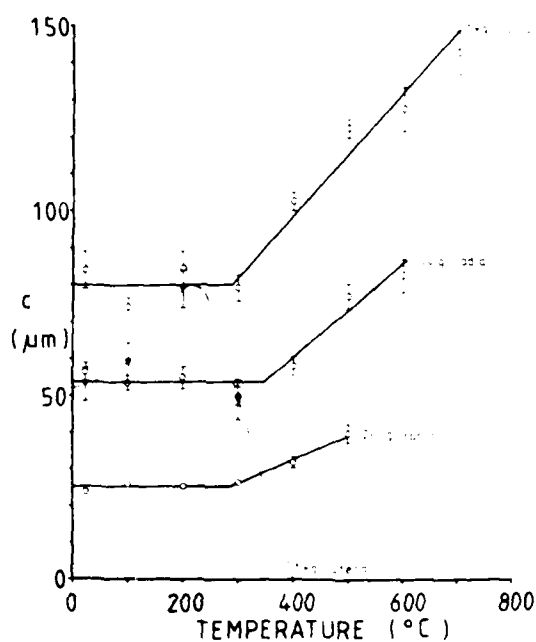


Figure 12. Radial and lateral crack radii as functions of temperature and load for n-type (111) single crystal Si: open circles-radial cracks, filled triangles-lateral cracks. Error bars indicate one standard error in the mean.

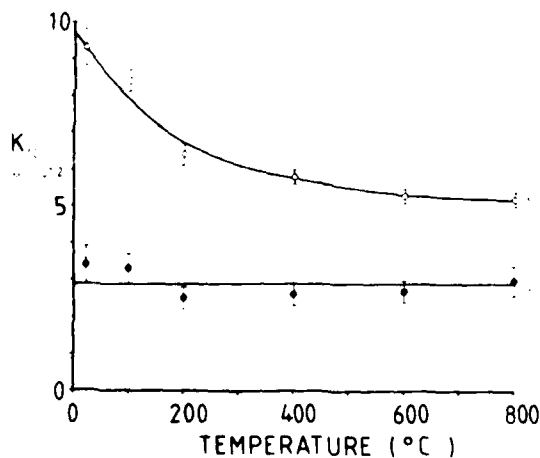


Figure 13. The effect of including a plastic zone size term in the calculation of K_{IC} as a function of temperature for hot-pressed SiC: curve 1 = original theory (open circles), curve 2 = with plastic zone size term (filled circles). Error bars indicate one standard error in the mean.

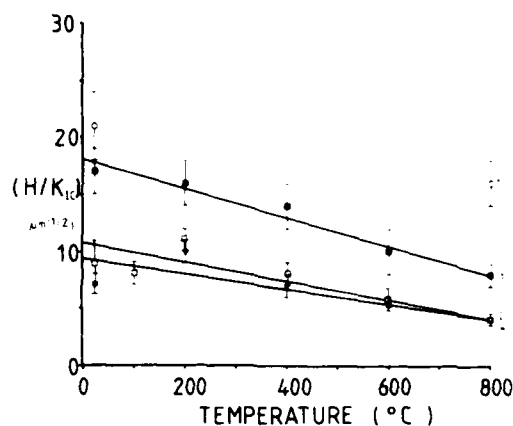


Figure 14. The variation of 'index of brittleness' (H/K_{IC}) with temperature for SiC materials: curve 1 = (0001) single crystal (open circles), curve 2 = NC203 hot-pressed (open squares), curve 3 = Carborundum sintered (filled squares), curve 4 = Suzuki sintered (open triangles). Error bars indicate one standard error in the mean.

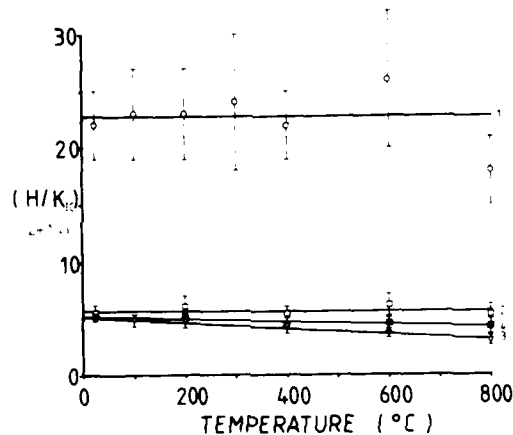


Figure 15. The variation of 'index of brittleness' (H/K_{IC}) with temperature for Si_3N_4 materials: curve 1 = PDSN (open circles), curve 2 = Ford '2.7' RBSN (open squares), curve 3 = NC132 hot-pressed (open triangles), curve 4 = NCX34 hot-pressed (filled squares). Error bars indicate one standard error in the mean.

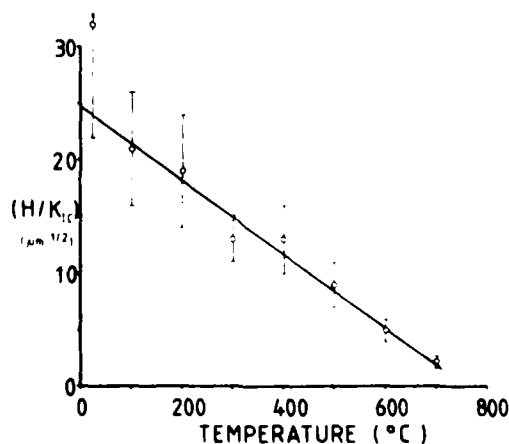


Figure 16. The variation of 'index of brittleness' (H/K_{IC}) with temperature for {111} single crystal Si. Error bars indicate one standard error in the mean.

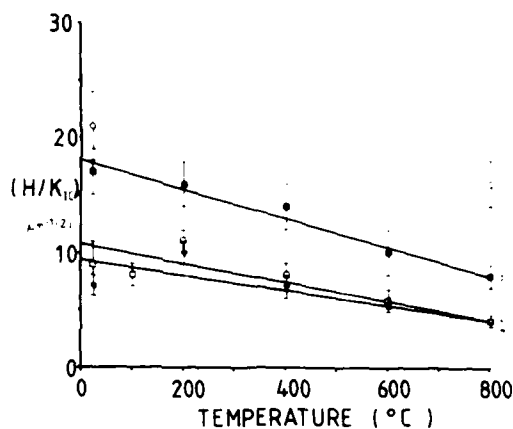


Figure 14. The variation of 'index of brittleness' (H/K_{IC}) with temperature for SiC materials: curve 1 = (0001) single crystal (open circles), curve 2 = NC203 hot-pressed (open squares), curve 3 = Carborundum sintered (filled squares), curve 4 = Suzuki sintered (open triangles). Error bars indicate one standard error in the mean.

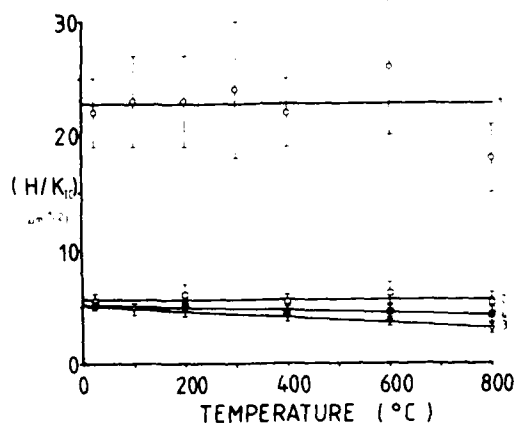


Figure 15. The variation of 'index of brittleness' (H/K_{IC}) with temperature for Si_3N_4 materials: curve 1 = PDSN (open circles), curve 2 = Ford '2.7' RBSN (open squares), curve 3 = NC132 hot-pressed (open triangles), curve 4 = NCX34 hot-pressed (filled squares). Error bars indicate one standard error in the mean.

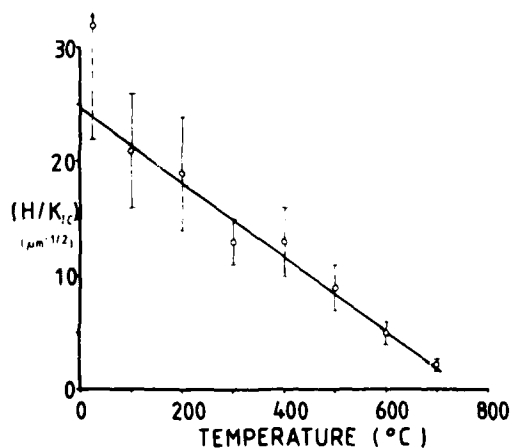


Figure 16. The variation of 'index of brittleness' (H/K_{IC}) with temperature for {111} single crystal Si. Error bars indicate one standard error in the mean.

END
DATE